ABSTRACT

LION, STEPHEN TODD. Control Authorities of a Distributed Actuation and Sensing Array on a Blended-Wing-Body Uninhabited Aerial Vehicle. (Under the direction of Dr. Charles Hall.)

A distributed actuation array was installed on a blended-wing-body uninhabited aerial vehicle and tested in the 12-foot subsonic wind tunnel at NASA's Langley Research Center. From the results of these tests, a discussion is given of the baseline aircraft, its conventional control surfaces, and the distributed array. Each effector in the distributed array was tested individually as well as pre-determined configurations incorporating all 12 effectors on each wing. From the tests on the individual effectors, a method was created that allows for the prediction of the control authorities for any configuration of the array. The six pre-determined shapes served as bases for comparison to determine the accuracy of the prediction scheme. Additionally, the shapes were compared to the conventional control surfaces to determine if a distributed array could completely replace those control surfaces.

Control Authorities of a Distributed Actuation and Sensing Array on a Blended-Wing-Body Uninhabited Aerial Vehicle

by

STEPHEN TODD LION

A thesis submitted to the Graduate Faculty of
North Carolina State University
in partial fulfillment of the
requirements for the Degree of
Master of Science

AEROSPACE ENGINEERING

Raleigh, North Carolina

2007

Approved by:

Dr. Charles E. Hall, Jr.
Chair of Advisory Committee

Dr. Ashok Gopalarathnam
Member of Advisory Committee

Dr. James F. Selgrade
Member of Advisory Committee

BIOGRAPHY

Stephen Todd Lion was born to Cathy and Steve Lion on March 18th, 1981 in Lancaster, California. The younger of two brothers, Todd grew up in Blowing Rock, NC, before attending college at NC State University in the fall of 1999. He graduated *cum laude* with a BS in Aerospace Engineering in the spring of 2003.

ACKNOWLEDGEMENTS

I would like to thank my advisor, Dr. Hall. I would also like to extend my gratitude toward my two committee members, Dr. Ashok Gopalarathnam and Dr. James Selgrade.

Dave Raney and Sue Grafton at NASA's Langley Research Center also deserve much appreciation, as they were the driving forces behind the wind tunnel testing of the aircraft used in this research. Will Barnwell, who designed and constructed the wings used in this project, also deserves many thanks.

Contents

List of Tables **vii**

List of Figures **viii**

Nomenclature **xiii**

1 Introduction **1**

1.1 Morphing Wing Concepts 1

1.2 NASA/DARPA Smart Wing 3

1.3 Objectives of this Project 5

2 Experimental Approach **6**

2.1 Wind Tunnel 6

2.2 MESA Testbed 7

2.2.1 *Thunderstruck* UAV 7

2.2.2 Wing Panels 8

2.2.3 Pressure Measurement System 11

2.2.4 Assembled MESA Testbed 12

2.2.5 Effector Control Interface 12

2.3 MESA Pressure Distribution 13
2.3.1 Methods 13
2.3.2 Results 14
2.4 Simple Section Lift Approximation 16
2.4.1 Method 16
2.4.2 Implementation on the MESA Platform 17
2.5 Testing Schedule 19
2.5.1 Baseline Aircraft and Conventional Control Surfaces 19
2.5.2 Individual Effectors 19
2.5.3 Effector Shapes 20

3 Data Analysis **23**
3.1 Baseline Aircraft 23
3.2 Conventional Control Surfaces 24
3.3 MESA Effectors 26
3.3.1 Individual Effectors 26
3.3.2 Effector Shapes 28

4 Prediction Methods **37**
4.1 Lift, Pitch, and Roll 37
4.1.1 Angles of Attack of $+4^\circ$, $+6^\circ$, and $+8^\circ$ 37
4.1.2 All Other Angles of Attack 40
4.2 Drag and Yaw 41
4.2.1 Second Degree Polynomial Scheme 41
4.2.2 Gauss Interpolation Scheme 44

5 Concluding Remarks **46**

5.1 Summary of Results 46

5.2 Recommendations for Future Work 48

6 Tables **49**

Bibliography **54**

Appendices **56**

A MESA Shape Authorities and Predictions for C_L, C_m, and C_l **57**

B MESA Shape Authorities and Predictions for C_D and C_n **64**

C MESA Shape Predictions for C_D Using Yaw Method **71**

List of Tables

6.1 Control powers for conventional control surfaces (deg^{-1}). 49

6.2 Lift, pitch, and roll control powers for right wing effectors (deg^{-1}). . 50

6.3 Lift, pitch, and roll control powers for left wing effectors (deg^{-1}). . . . 51

6.4 Linear curve fit data for right wing effectors with α variation. 52

6.5 Linear curve fit data for left wing effectors with α variation. 53

List of Figures

2.1 NASA Langley 12-Foot Subsonic Wind Tunnel. 7

2.2 CAD models and photographs of *Thunderstruck UAV.* 8

2.3 Completed MESA wing panel for starboard wing. 9

2.4 Effector dimensions. 10

2.5 Prototype build of pull-pull servo linkages for effector. 10

2.6 Example trailing edge deflection configurations shown on port wing. . 10

2.7 Location of pressure tap upstream of effector. 11

2.8 Assembled MESA testbed with effector arrays installed. 12

2.9 Pressure responses for effectors #4-#8 for a deflection of effector #6. 14

2.10 Predicted and experimental pressure responses. 16

2.11 Comparison of simple lift approximation and wing theory. 18

2.12 Effector deflection configurations tested on the MESA platform. . . . 21

3.1 Pitching moment and lift curves for baseline MESA platform. 24

3.2 Rolling moments for anti-symmetric aileron deflections. 25

3.3 Yawing and rolling moments for rudder deflections. 25

3.4 Pitching moment and lift for symmetric elevon deflections. 26

3.5 Pitching moment and lift for symmetric aileron deflections. 26

3.6 Pitching moment coefficients for right wing effectors at $\alpha = 4\,^{\circ}$. 27
3.7 Pitching moment coefficients for left wing effectors at $\alpha = 4\,^{\circ}$. 27
3.8 Pitching moment and lift curves for symmetric shape 1. 29
3.9 Rolling moment curves for anti-symmetric shape 1. 29
3.10 Pitching moment and lift curves for symmetric shape 2. 29
3.11 Rolling moment curves for antisymmetric shape 2. 29
3.12 Pitching moment and lift curves for symmetric shape 3. 30
3.13 Rolling moment curves for anti-symmetric shape 3. 30
3.14 Drag coefficient comparison for symmetric shapes 1 and 2. 30
3.15 Drag coefficient comparison for anti-symmetric shapes 1 and 2. 30
3.16 Drag coefficient comparison for symmetric shapes 1 and 3. 31
3.17 Drag coefficient comparison for anti-symmetric shapes 1 and 3. 31
3.18 Drag coefficient comparison for symmetric shapes 2 and 3. 31
3.19 Drag coefficient comparison for anti-symmetric shapes 2 and 3. 31
3.20 Lift to drag ratio for shapes 1, 2, and 3 at $\alpha = +6\,^{\circ}$. 32
3.21 Rolling moment to drag ratio for anti-symmetric shapes 1, 2, and 3. . 33
3.22 Pitching moment to drag ratio for symmetric shapes 1, 2, and 3. . . . 33
3.23 Drag coefficients for right wing effectors for shapes 4, 5, and 6. 34
3.24 Drag coefficients for left wing effectors for shapes 4, 5, and 6. 34
3.25 Yawing moment coefficients for right wing shapes 4, 5, and 6. 35
3.26 Yawing moment coefficients for left wing shapes 4, 5, and 6. 35
3.27 Pitch moment and lift coefficients for right wing shapes 4, 5, and 6. . 36
3.28 Pitch moment and lift coefficients for left wing shapes 4, 5, and 6. . . 36
3.29 Rolling moment coefficients for right wing shapes 4, 5, and 6. 36
3.30 Rolling moment coefficients for left wing shapes 4, 5, and 6. 36

4.1 Comparison of drag for left wing effectors 10 and 11 at $\alpha = 4\,^\circ$ 42

A.1 Predictions of lift, pitch, and roll for sym. shape 1, $\alpha = +4\,^\circ$. 57
A.2 Predictions of lift, pitch, and roll for sym. shape 1, $\alpha = +6\,^\circ$. 57
A.3 Predictions of lift, pitch, and roll for sym. shape 1, $\alpha = +8\,^\circ$. 58
A.4 Predictions of lift, pitch, and roll for anti-sym. shape 1, $\alpha = +4\,^\circ$. . . 58
A.5 Predictions of lift, pitch, and roll for anti-sym. shape 1, $\alpha = +6\,^\circ$. . . 58
A.6 Predictions of lift, pitch, and roll for anti-sym. shape 1, $\alpha = +8\,^\circ$. . . 58
A.7 Predictions of lift, pitch, and roll for sym. shape 2, $\alpha = +4\,^\circ$. 59
A.8 Predictions of lift, pitch, and roll for sym. shape 2, $\alpha = +6\,^\circ$. 59
A.9 Predictions of lift, pitch, and roll for sym. shape 2, $\alpha = +8\,^\circ$. 59
A.10 Predictions of lift, pitch, and roll for anti-sym. shape 2, $\alpha = +4\,^\circ$. . . 59
A.11 Predictions of lift, pitch, and roll for anti-sym. shape 2, $\alpha = +6\,^\circ$. . . 59
A.12 Predictions of lift, pitch, and roll for anti-sym. shape 2, $\alpha = +8\,^\circ$. . . 59
A.13 Predictions of lift, pitch, and roll for sym. shape 3, $\alpha = +4\,^\circ$. 60
A.14 Predictions of lift, pitch, and roll for sym. shape 3, $\alpha = +6\,^\circ$. 60
A.15 Predictions of lift, pitch, and roll for sym. shape 3, $\alpha = +8\,^\circ$. 60
A.16 Predictions of lift, pitch, and roll for anti-sym. shape 3, $\alpha = +4\,^\circ$. . . 60
A.17 Predictions of lift, pitch, and roll for anti-sym. shape 3, $\alpha = +6\,^\circ$. . . 60
A.18 Predictions of lift, pitch, and roll for anti-sym. shape 3, $\alpha = +8\,^\circ$. . . 60
A.19 Predictions of lift, pitch, and roll for left wing shape 4, $\alpha = +4\,^\circ$. . . . 61
A.20 Predictions of lift, pitch, and roll for left wing shape 4, $\alpha = +6\,^\circ$. . . . 61
A.21 Predictions of lift, pitch, and roll for left wing shape 4, $\alpha = +8\,^\circ$. . . . 61
A.22 Predictions of lift, pitch, and roll for right wing shape 4, $\alpha = +4\,^\circ$. . . 61
A.23 Predictions of lift, pitch, and roll for right wing shape 4, $\alpha = +6\,^\circ$. . . 61

A.24 Predictions of lift, pitch, and roll for right wing shape 4, $\alpha = +8\,^\circ$. . . 61
A.25 Predictions of lift, pitch, and roll for left wing shape 5, $\alpha = +4\,^\circ$. . . . 62
A.26 Predictions of lift, pitch, and roll for left wing shape 5, $\alpha = +6\,^\circ$. . . . 62
A.27 Predictions of lift, pitch, and roll for left wing shape 5, $\alpha = +8\,^\circ$. . . . 62
A.28 Predictions of lift, pitch, and roll for right wing shape 5, $\alpha = +4\,^\circ$. . . 62
A.29 Predictions of lift, pitch, and roll for right wing shape 5, $\alpha = +6\,^\circ$. . . 62
A.30 Predictions of lift, pitch, and roll for right wing shape 5, $\alpha = +8\,^\circ$. . . 62
A.31 Predictions of lift, pitch, and roll for left wing shape 6, $\alpha = +4\,^\circ$. . . . 63
A.32 Predictions of lift, pitch, and roll for left wing shape 6, $\alpha = +6\,^\circ$. . . . 63
A.33 Predictions of lift, pitch, and roll for left wing shape 6, $\alpha = +8\,^\circ$. . . . 63
A.34 Predictions of lift, pitch, and roll for right wing shape 6, $\alpha = +4\,^\circ$. . . 63
A.35 Predictions of lift, pitch, and roll for right wing shape 6, $\alpha = +6\,^\circ$. . . 63
A.36 Predictions of lift, pitch, and roll for right wing shape 6, $\alpha = +8\,^\circ$. . . 63

B.1 Predictions of drag for symmetric shape 1. 64
B.2 Predictions of drag for anti-symmetric shape 1. 64
B.3 Predictions of drag for symmetric shape 2. 65
B.4 Predictions of drag for anti-symmetric shape 2. 65
B.5 Predictions of drag for symmetric shape 3. 65
B.6 Predictions of drag for anti-symmetric shape 3. 65
B.7 Predictions of drag for left wing shape 4. 66
B.8 Predictions of drag for right wing shape 4. 66
B.9 Predictions of drag for left wing shape 5. 66
B.10 Predictions of drag for right wing shape 5. 66
B.11 Predictions of drag for left wing shape 6. 67

B.12 Predictions of drag for right wing shape 6. 67
B.13 Predictions of yaw for symmetric shape 1. 67
B.14 Predictions of yaw for anti-symmetric shape 1. 67
B.15 Predictions of yaw for symmetric shape 2. 68
B.16 Predictions of yaw for anti-symmetric shape 2. 68
B.17 Predictions of yaw for symmetric shape 3. 68
B.18 Predictions of yaw for anti-symmetric shape 3. 68
B.19 Predictions of yaw for left wing shape 4. 69
B.20 Predictions of yaw for right wing shape 4. 69
B.21 Predictions of yaw for left wing shape 5. 69
B.22 Predictions of yaw for right wing shape 5. 69
B.23 Predictions of yaw for left wing shape 6. 70
B.24 Predictions of yaw for right wing shape 6. 70

C.1 Predictions of drag for left wing shape 4 using yaw method. 71
C.2 Predictions of drag for right wing shape 4 using yaw method. 71
C.3 Predictions of drag for left wing shape 5 using yaw method. 72
C.4 Predictions of drag for right wing shape 5 using yaw method. 72
C.5 Predictions of drag for left wing shape 6 using yaw method. 72
C.6 Predictions of drag for right wing shape 6 using yaw method. 72

Nomenclature

b	wingspan
C_D	aircraft drag coefficient
C_L	aircraft lift coefficient
C_l	aircraft rolling moment coefficient, airfoil lift coefficient
C_m	aircraft pitching moment coefficient
C_n	aircraft yawing moment coefficient
C_P	pressure coefficient
C_Y	aircraft side force coefficient
q	dynamic pressure
α	angle of attack
β	sideslip angle
δ	control surface deflection angle

Subscripts

$Baseline$	coefficients with no control surface deflections
$Effector$	coefficient created by a single MESA effector
f	flap/effector
$Lower$	airfoil lower surface
$Measured$	coefficients with deflected control surfaces
$Upper$	airfoil upper surface
X	any aircraft control coefficient

Abbreviations/Acronyms

BWB	Blended-wing-body
DARPA	Defense Advanced Research Projects Agency
LaRC	Langley Research Center
MESA	Multifunctional effector and sensor array
NASA	National Aeronautics and Space Administration
NGC	Northrop Grumman Corporation
SMA	Shape memory alloy
TEL	Trailing edge left
TER	Trailing edge right
UAV	Uninhabited aerial vehicle
UCAV	Uninhabited combat aerial vehicle

Chapter 1

Introduction

1.1 Morphing Wing Concepts

In recent years, research has been conducted on the concept of the morphing wing. The definition of the term "morphing wing," as provided by the National Aeronautics and Space Administration (NASA), is a wing that utilizes

> *efficient, multi-point adaptability* and may include very small or large vehicle changes and structural and/or fluidic approaches. In defining "morphing" in this manner, *efficient* denotes mechanically simpler, lighter weight, and/or more energy efficient than conventional systems; *multi-point* denotes accommodating diverse (and sometimes contradictory) mission scenarios; and *adaptability* denotes extensive versatility and resilience to varying conditions or problems.[1]

In this manner, one could design a wing that could change its planform or airfoil shapes to attain optimal aerodynamic efficiency at each point in the aircraft's flight envelope. Traditional designs for aircraft have incorporated compromise between optimal designs for each regime of flight. A highly swept wing with a diamond airfoil may be the optimal shape for the supersonic regime of a fighter jet's flight envelope, but these characteristics may be completely unsuitable for takeoff and landing. Thus, a compromise must be reached between the many critical flight regimes, often at the expense of efficiency at each one. The morphing wing seeks to solve this problem by allowing the wing to operate at its optimal geometry at each stage of flight. One example that has been theorized involves using unique fuel containers within the wing that allow for the airfoil to morph from a bulky state to a sleeker one as fuel is burned and interior space is created from the shrinking of the fuel bladders.[2] Another example that has been studied incorporates a wing which has an upper surface that can detach and form a sort of bi-plane for high maneuverability regimes of flight. The upper wing can reattach to the main wing for cruise and allow for optimization for range or endurance.[3]

Aircraft utilizing morphing technologies will ultimately no longer have to sacrifice performance at any flight regime. These optimizations can result in less drag over the entire flight envelope, thereby reducing the needed thrust and consumed fuel for the aircraft.

Inspirations vary for what route to follow when designing these wings, but one that has drawn a large amount of interest is biology.[1] The Biologically Inspired Smart Nanotechnology research group at NASA's Langley Research Center (LaRC) is comprised of engineers and researchers involved with creating biologically inspired mate-

rials. One such material that has already been fabricated is a lightweight, electrically responsive material that can be used as a wing skin and act as its own controlling mechanism for fine, dynamic control of the wing. Efforts have also been taken to expand this research to include piezoelectric materials that can both sense surface pressures and actuate to morph the wing surface to the desired shape for any given airflow.[1] Other examples of larger, coordinated efforts to develop morphing aircraft can be found it NASA's Aircraft Morphing Program and the Defense Advanced Research Projects Agency's (DARPA) Morphing Aircraft Structures Program.[4]

1.2 NASA/DARPA Smart Wing

The Smart Wing program, conducted by a team led by the Northrop Grumman Corporation (NGC) in conjunction with DARPA, NASA, and the Air Force Research Laboratories, is one of the most visible forays into morphing wing research. The Smart Wing project was comprised of two phases, each with two series of wind tunnel tests at NASA LaRC. Phase 1 (January 1995 to February 1999) consisted of a 16% scale model of a wing from an advanced military fighter. This wing incorporated contoured, hingeless flap and aileron designs based on shape-memory alloys (SMA) as well as wing twist actuated by an internal torque tube. Wind tunnel tests in Phase 2 (January 1997 to November 2001) were conducted on a 30% scale model of an NGC uninhabited combat aerial vehicle (UCAV) which added contoured leading-edge slats to the technologies used in Phase 1.

The wing used in Phase 1 of the Smart Wing project[5] incorporated three advanced morphing characteristics. The SMA-actuated, trailing edge control surfaces had a

maximum deflection of 10° and could be configured in a variety of spanwise configurations. The torque-actuated wing twist could achieve a twist of 5°. In comparison to a test wing of equal parameters with conventional, hinged control surfaces, the Smart Wing saw improvements of 8-17% in lift and roll authority. It has been shown[5],[6] that wings utilizing contoured control surfaces obtain improved pressure and flow characteristics over the control surface. The smooth transition prevents abrupt changes in pressure and can offset stall to higher deflections or angles of attack, therefore increasing the effectiveness of the control surface. For example, the wind tunnel tests of Phase 1 of the Smart Wing showed a 10% increase in rolling moment created by a 10° deflection of the Smart aileron compared to a 10° deflection of a conventional aileron at an angle of attack of 8°. Additionally, a 7.5° deflection of both Smart flaps and ailerons produced at 17.6% increase in lift from the conventional wing.

The UCAV created for Phase 2 of the project incorporated much of the same technology as Phase 1 with the additions of contoured, leading-edge slats and faster-response piezoelectric control surfaces.[7] One of the largest disadvantages of the SMA control surfaces used in Phase 1 is that they take several seconds to deploy and even longer to return to zero deflection, relying solely on the airflow for passive cooling[5] – this shortcoming was remedied in Phase 2 with deflection rates of up to $80°/s$.[7] Phase 2 incorporated wind-tunnel testing into the transonic regime at dynamic pressures of up to 300 psf in the NASA LaRC transonic-dynamic tunnel.[8]

1.3 Objectives of this Project

The motivations behind this project are much the same as those behind most morphing wing projects. Due to technical and financial limitations, the distributed actuation system for this project is comprised of multiple, discrete control surfaces, instead of the more advanced systems found on the Smart Wing. This project utilizes a multifunctional effector and sensor array (MESA) installed on the trailing edges of the wings of a blended-wing-body (BWB) uninhabited aerial vehicle (UAV). The UAV was created at NC State University and later modified to accommodate the MESA effectors. Six weeks of extensive wind-tunnel testing on the assembled model was performed at the LaRC 12-foot subsonic tunnel. The data from this testing are analyzed to determine the characteristics of the aircraft, its conventional control surfaces, and the MESA effectors. Several pre-designated configurations of the distributed array were tested, along with each individual MESA control surface. Using the data from the individual effectors, a scheme will be created to predict the control authority of any configuration of the array. The results from the pre-designated configurations will be used as a basis for comparison to determine the accuracy of the prediction scheme.

Chapter 2

Experimental Approach

A series of tests was run on the MESA platform over a total of six weeks in the summers of 2003 and 2004 in the 12-foot, subsonic wind tunnel at NASA LaRC.

2.1 Wind Tunnel

The NASA Langley 12-Foot Subsonic Wind Tunnel, operated by the Vehicle Dynamics Branch of the Airborne Systems Competency, is an atmospheric pressure, open return tunnel with an octagonal test section measuring 12 ft across and 15 ft in length contained within a 60 ft diameter sphere (Figure 2.1). Each side of the test section octagon measures 5 ft. The maximum operating dynamic pressure (q) of the tunnel is 7 lb/ft^2, which equates to 77 ft/s at standard sea level density and a Reynolds number of approximately 490,000 ft^{-1}. All runs with the MESA testbed installed were at an operating q of 5 psf, or 65 ft/s at standard conditions. The aircraft's designed cruise speed is 117 ft/s, but the velocity had to be lowered in the

tunnel because of rapid heating of the fan motor at higher speeds due to the model's high blockage of the test section.

Figure 2.1: NASA Langley 12-Foot Subsonic Wind Tunnel.

2.2 MESA Testbed

2.2.1 *Thunderstruck* UAV

The MESA testbed was created from a BWB UAV designed and constructed at NC State University as a senior design project in aerospace engineering during the 2001-2002 school year. The aircraft, named *Thunderstruck*, shown in Figure 2.2, shares its general planform shape with the NASA BWB design[9]. The aircraft[10] is composed from a NACA 0015 airfoil with a 58 *in* root chord tapering to a 5.25 *in* tip chord with

a mean aerodynamic chord of 34.3 *in*. The UAV has a wing area of 17.77 ft^2 over its 9.38 ft wingspan. The aircraft is powered by an Aviation Microjet Technology™ AT180 mini-turbojet engine rated at 15 lbf static thrust. The aircraft has a dry weight of 30 lb with capacity for a 15 lb payload. The aircraft is dolly-launched and skid-landed, so conventional landing gear is not required on the airframe.

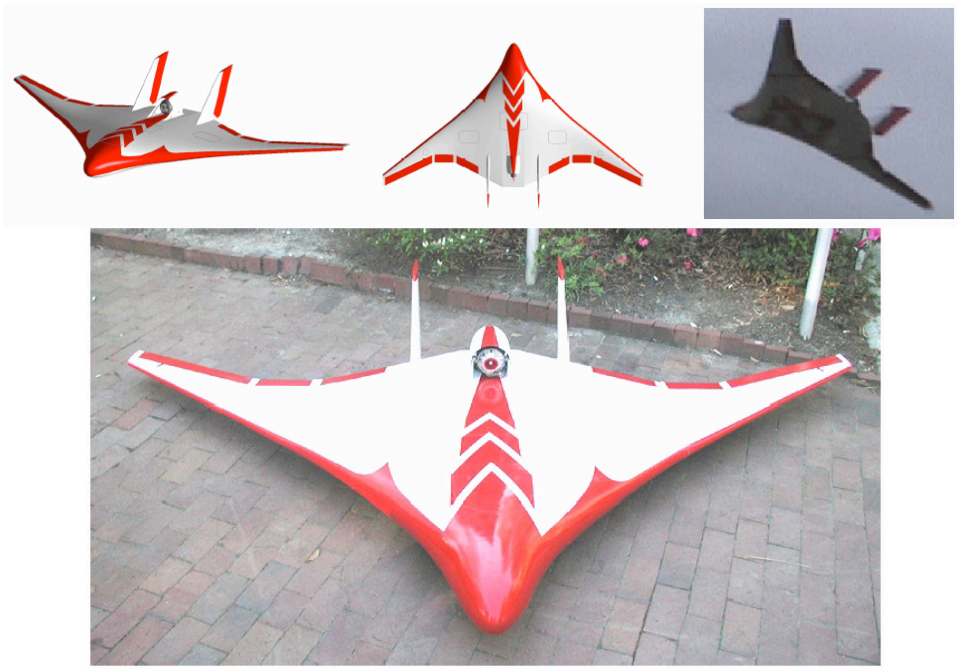

Figure 2.2: CAD models and photographs of *Thunderstruck UAV*.[10]

2.2.2 Wing Panels

Modifications specific to the MESA testbed[6] consisted of replacing the outboard wing sections with custom-built sections containing the effector array. The outer 31.25 *in* of wing (21 *in* root chord, 5.25 *in* tip chord) were replaced with new sections capable of housing the effector and sensor array. A change in sweep occurs 9 *in*

from the root of the section. Twelve effectors are located on each wing, with the first effector located at the root of the wing section and the twelfth effector located 18 *in* from the root. Six effectors are located before the break in sweep angle. The effectors on each wing are numbered 1 through 12, with 1 being the most inboard and all other numbered sequentially. Due to the change in sweep angle, effector #7 is slightly smaller than the other 11 effectors. The outboard section of wing houses a conventional hinged control surface. The completed wing section can be seen in Figure 2.3.

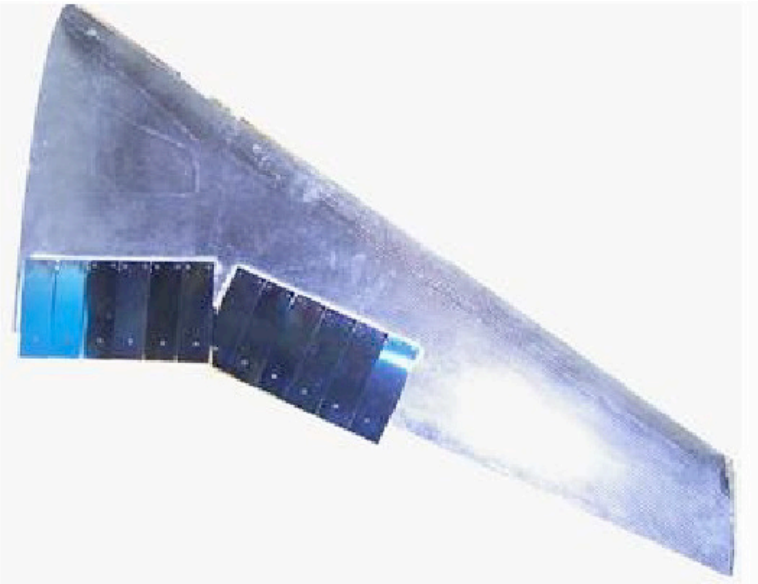

Figure 2.3: Completed MESA wing panel for starboard wing.[6]

Each effector has dimensions of 0.007 *in* (thickness), 1.5 *in* (width), and 4 *in* (length) and is created from two rectangular elements of spring steel (Figure 2.4). The attachment scheme of the spring steel allows the effectors to deflect in the fashion of a contoured, hingeless control surface. Each effector is actuated by a pull-pull mechanism driven by a Hobbico^{TM} CS-5 nano-servo, as shown in Figure 2.5. Each effector

is capable of fully independent motion with deflections of $\pm 15^\circ$ at a maximum rate of greater than 2 Hz. Some examples of effector deflections are shown in Figure 2.6.

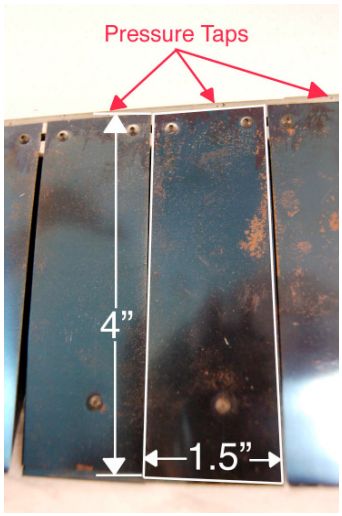

Figure 2.4: Effector dimensions.

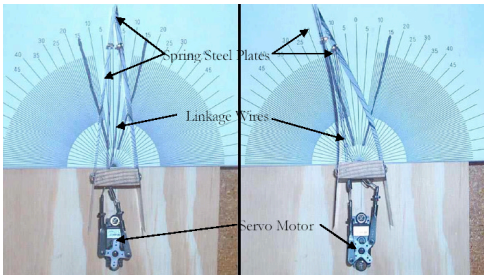

Figure 2.5: Prototype build of pull-pull servo linkages for effector.[6]

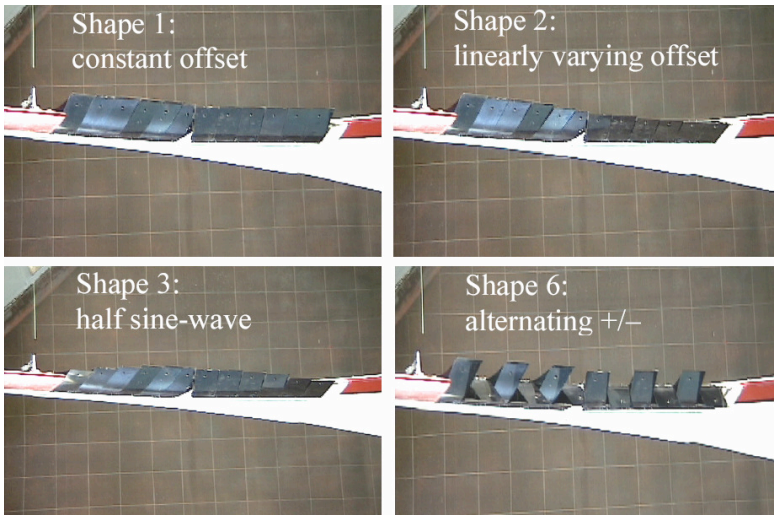

Figure 2.6: Example trailing edge deflection configurations shown on port wing.[11]

2.2.3 Pressure Measurement System

The modified wing sections also incorporate a single surface pressure tap placed 4.05 *in* from the trailing edge of each effector on the upper surface, giving a total of 24 sensors across the two wings. Figures 2.4 and 2.7 show the locations of the 0.040 *in* diameter pressure taps. Each pressure tap is located 0.75 *in* from the edge of its paired effector, immediately forward of the center of the effector. The tubulations are connected to the pressure monitoring system by 0.040 *in* diameter nylon tubing. The pressures were monitored by a Pressure Systems Inc.^{TM} ESP 32HD electronic scanning pressure module.

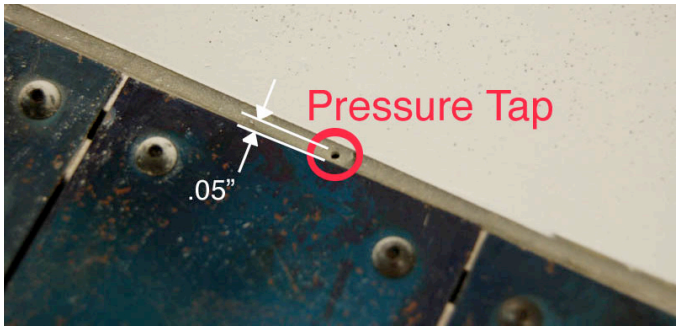

Figure 2.7: Location of pressure tap upstream of effector.

The ESP module was placed inside the test model to minimize the length of the tubing between the pressure taps and the ESP device. The module was also placed inside a thermostatically controlled heater box to eliminate the influence of temperature variations within the tunnel on the pressure transducers. The ESP has a pressure measurement range of ± 10 *in* H_2O and is capable of electronically multiplexing up to 32 independent pressure measurements. Pressure measurements from the 24 taps on the model were scanned and multiplexed by the ESP at a 1.5 *ms* time interval, so the measurement at each tap was updated every 36 *ms*.

2.2.4 Assembled MESA Testbed

The MESA testbed can be seen in Figure 2.8. Control surface configuration on this aircraft is as follows: elevons (most inboard), MESA array, and ailerons (most outboard), with conventional rudders on the vertical tails.

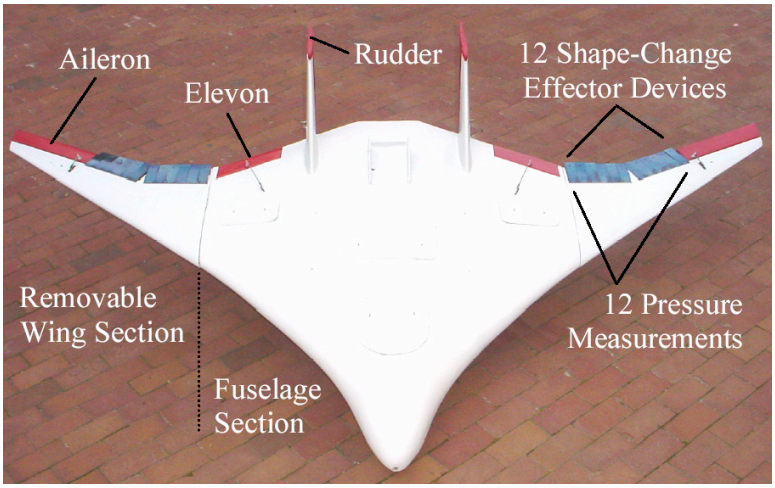

Figure 2.8: Assembled MESA testbed with effector arrays installed.[11]

2.2.5 Effector Control Interface

The pressure measurement and effector control interface[11] for use in the Langley wind tunnel was designed and implemented using dSpace™ hardware-in-the-loop computer components and software together with MATLAB Simulink™ and Real-Time Workshop™. The dSpace™ interface allows for control of all moveable surfaces on the model with open-loop commands as well as closed-loop signals from the pressure or bank angle controller. Four BASIC-X™ servo serial boards were located within the model to translate the dSpace™ position commands to pulse train signals

for the effector servos. Each board can control up to eight servos and was controlled remotely from the dSpace^{TM} serial connections using the RS232 protocol.

2.3 MESA Pressure Distribution

2.3.1 Methods

Previous research[6] at NC State on the MESA wing panels has shown that the spanwise pressure distribution along the effector array can be accurately predicted by multiplication of a pressure sensitivity matrix with a deflection vector. Testing for the pressure distribution was performed one wing at a time in the NCSU subsonic wind tunnel. The outer wing panels were attached to a splitter plate to eliminate the effects of the boundary layer on the wind tunnel wall, and the pressures were measured with a Scanivalve^{TM} system.

Each effector was tested individually over a full deflection (δ) range of $-15\,^{\circ}$ to $+15\,^{\circ}$. At each of these points, pressures were recorded from each of the 12 pressure taps. From these data, a linear response was found at each effector for every other effector's deflection. Figure 2.9 shows the responses of effectors $\#4 - \#8$ to a deflection of effector #6, where ΔC_P is defined as:

$$\Delta C_P = \Delta C_{P_{Measured}} - \Delta C_{P_{Baseline}} \tag{2.1}$$

Obviously, the pressures at effector #6 are affected most by its own deflection, but the deflection of effector #6 also induces a change in pressure at every other effector

in the array. Effectors #5 and #7 are affected the most, followed by #4 and #8, and so on.

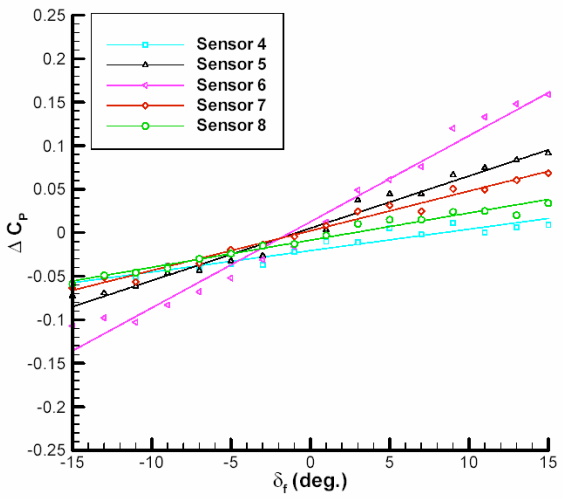

Figure 2.9: Pressure responses for effectors #4-#8 for a deflection of effector #6.[6]

2.3.2 Results

The change in ΔC_P over the deflection range was found to be very linear. This observation holds true for all effectors. Thus, a matrix of pressure sensitivities can be created for each wing. When deflecting more than one effector, the pressure response at any pressure tap can be found by simply summing the effects on that pressure tap of each effector:

$$Ax = b \tag{2.2}$$

where A is the pressure sensitivity matrix, x a vector of effector deflections, and b is the resulting ΔC_P at each pressure tap:

$$A = \begin{bmatrix} \left(\frac{d(\Delta C_P)}{d\delta_f}\right)_{11} & \left(\frac{d(\Delta C_P)}{d\delta_f}\right)_{12} & \cdots & \left(\frac{d(\Delta C_P)}{d\delta_f}\right)_{1N} \\ \left(\frac{d(\Delta C_P)}{d\delta_f}\right)_{21} & \left(\frac{d(\Delta C_P)}{d\delta_f}\right)_{22} & \cdots & \left(\frac{d(\Delta C_P)}{d\delta_f}\right)_{2N} \\ \vdots & \vdots & \ddots & \vdots \\ \left(\frac{d(\Delta C_P)}{d\delta_f}\right)_{N1} & \left(\frac{d(\Delta C_P)}{d\delta_f}\right)_{N2} & \cdots & \left(\frac{d(\Delta C_P)}{d\delta_f}\right)_{NN} \end{bmatrix} \tag{2.3}$$

$$x = \begin{bmatrix} \delta_{f1} \\ \delta_{f2} \\ \vdots \\ \delta_{fN} \end{bmatrix} \tag{2.4}$$

$$b = \begin{bmatrix} \Delta C_{P_1} \\ \Delta C_{P_2} \\ \vdots \\ \Delta C_{P_N} \end{bmatrix} \tag{2.5}$$

Using this method, accurate predictions for pressure distributions can be made for any effector configuration. Figure 2.10 shows the measured and predicted pressure response for a sinusoidal effector configuration. The predicted pressures match up very well to the pressures read from the pressure taps during wind-tunnel testing. Barnwell showed that this level of accuracy was consistent for many different effector configurations, and it would follow that the method would work for any effector configuration.

This method can be applied to many scenarios in which a prescribed spanwise pressure distribution might be beneficial. Research has shown that spanwise camber variation can be tailored to produce a lift distribution to minimize induced drag.[12] Additionally, this method can be applied to minimize the root bending moment of the wing, thereby reducing weight and cost. In order to perform a bending moment analysis, though, one must be able to determine the lift coefficient for each cross-section of the wing; a method for this is detailed in the following section.

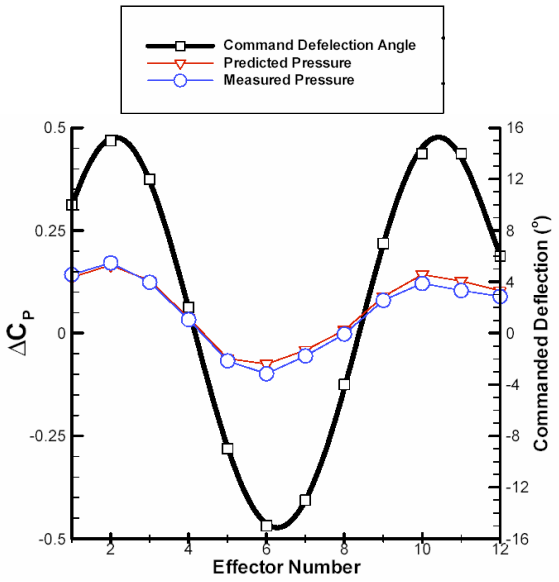

Figure 2.10: Predicted and experimental pressure responses to a sinusoidal effector configuration.[6]

2.4 Simple Section Lift Approximation

2.4.1 Method

Recent research[13] at the Ohio State University has shown that section lift coefficients can be accurately measured with as few as two chordwise pressure taps. Conventional methods for calculating section lift coefficients involve a large number of pressure taps along the chord of an airfoil for use in numerical integration. This method greatly reduces the calculation time and instrumentation that would be required for the integration method.

Knowing the airfoil geometry and flight velocity, a 2-dimensional CFD program such as XFOIL™ can be used to create a model for behavior of pressures at specific

points on the airfoil's surface. Two points can be chosen as these locations, one on the upper surface and one on the lower surface at the same chordwise location, preferably between 30% and 40% from the leading edge. The pressures at these locations can be withdrawn from the CFD results at each simulated angle of attack and transformed into ΔC_P using equation 2.6.

$$\Delta C_P = \Delta C_{P_{Lower}} - \Delta C_{P_{Upper}} \tag{2.6}$$

For pre-stall angles of attack, the relationship between ΔC_P and section lift coefficient C_l is found to be linear:

$$C_l = A + B(\Delta C_P) \tag{2.7}$$

where A and B are airfoil-specific constants drawn from the theoretical linear fit curve.

Once this equation has been established, it can be used in a physical system with high accuracy to determine section lift coefficient. This method was used on a sample wing in Ohio State's 3x5 foot subsonic wind tunnel with a high level of accuracy.[13] Figure 2.11 shows the section lift for two wind tunnel tests as predicted by this method (with and without grit) compared to conventional wing theory.

2.4.2 Implementation on the MESA Platform

On the MESA platform, a variation of this method can be used, despite the limitation of having only one pressure reading for each airfoil section. A similar method can

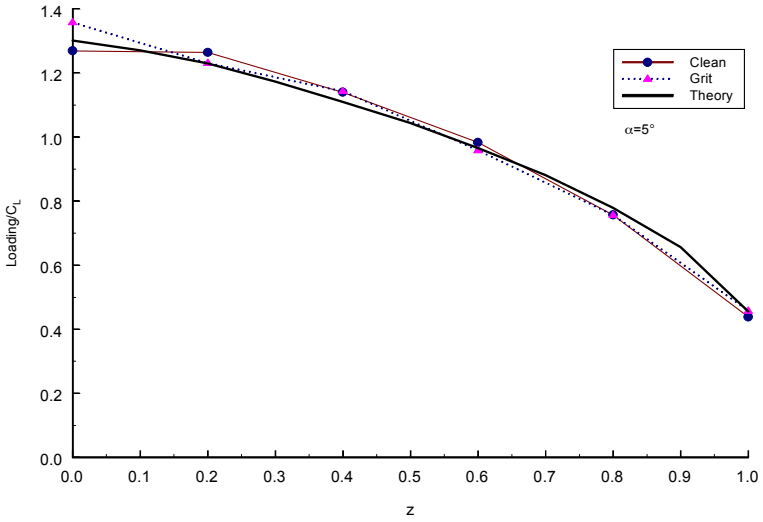

Figure 2.11: Comparison between simple lift approximation from wind tunnel tests and conventional wing theory.[13]

be created for use with a single pressure tap system, with the only difference being that the linear relationship must be found using C_P instead of ΔC_P. This results in a loss of accuracy that would preferably be avoided and can be if consideration for this method is taken into account during the design and construction of a flight model.

Another limitation of implementation of this method on the MESA platform is the chordwise location of the pressure taps. The most accurate data results from the taps being placed at chordwise locations between 30% and 40%, but on the MESA platform, all pressure taps are located 4.05 *in* from the trailing edge of the wing. Over the span of the MESA effectors, the pressure taps are located between 40% for the outboard and 80% for the inboard effectors. The section lift approximation breaks down as the pressure readings move toward the trailing edge, and it would not be able to be accurately utilized on this particular setup of the MESA platform.

2.5 Testing Schedule

2.5.1 Baseline Aircraft and Conventional Control Surfaces

Testing of the MESA platform in the Langley 12-foot wind tunnel began with a simple angle of attack (α) sweep of -2° to $+20^\circ$ in increments of 2° at zero sideslip (β). Following this was a series of β runs from -5° to $+5^\circ$ at $\alpha's$ of -2° to $+20^\circ$ in 2° increments. The final baseline run was a higher resolution α sweep at zero sideslip, again from -2° to $+20^\circ$ but in increments of 1°. The three tests were averaged to form the baseline run which will be used to find the control powers for all effectors.

The conventional control surfaces were tested next, all at zero sideslip and an angle of attack range of -2° to $+12^\circ$. The ailerons were tested in both anti-symmetric and symmetric configurations with deflection angles of -15° to $+15^\circ$. The elevons were tested in symmetric fashion over a δ range of $\pm 15^\circ$, as were the rudders over a $\pm 14^\circ$ range. Each of these runs will serve as a basis for comparison for all of the MESA configurations. These comparisons will determine if the MESA array is powerful enough to completely replace the conventional control surfaces.

2.5.2 Individual Effectors

Each effector was run through an entire $\pm 15^\circ$ δ sweep in 2° increments at each operating α of $+4^\circ$, $+6^\circ$, and $+8^\circ$. For these sweeps, only the desired effector was deflected; all other control surfaces were set to zero δ. The data collected from these runs will serve as the building blocks from which a comprehensive effector

configuration prediction scheme can be formulated. The aircraft performance will be recorded with each of these deflections, which may introduce some error due to the very small changes in performance due to the small size of the effectors.

2.5.3 Effector Shapes

Three elementary shapes (linear, sinusoid, and zigzag) were used as the basis for the six effector configurations, shown in Figure 2.12. Shape 1 refers to a deflection of all 12 effectors by the same angle, resulting in a straight horizontal line at the trailing edge that simulates a conventional control surface. Shape 2 is another variant of the linear shape; the control surfaces attempt to form a linear variation between effector #1 and #12. Shapes 3, 4, and 5 are all variants on the sine wave shape. Shape 3 is a half sine wave, shape 4 is one complete wave, and shape 5 is one and a half waves. Shape 6 couples each pair of effectors with opposite deflections of equal magnitude, resulting in a repeating "one up, one down" zigzag configuration.

Each of these configurations was tested over an α range of $+2^\circ$ to $+12^\circ$ in steps of 2°. Shapes 1, 2, and 3 were tested over $\delta's$ of -15° to $+15^\circ$ in increments of 3° at each α in both symmetric and anti-symmetric fashions. The terms "symmetric" and "anti-symmetric" refer to the relationship of the array deflection on the left wing and the array on the right wing. Shapes 4, 5, and 6 were only tested one wing at a time (e.g. deflected right wing effectors, non-deflected left wing effectors), as these were believed to be more inducing of drag, and subsequently yawing moment, than any other force or moment. Each configuration was tested as left wing only and right wing only over varying $\delta's$ ranging within $\pm 15^\circ$ at each angle of attack.

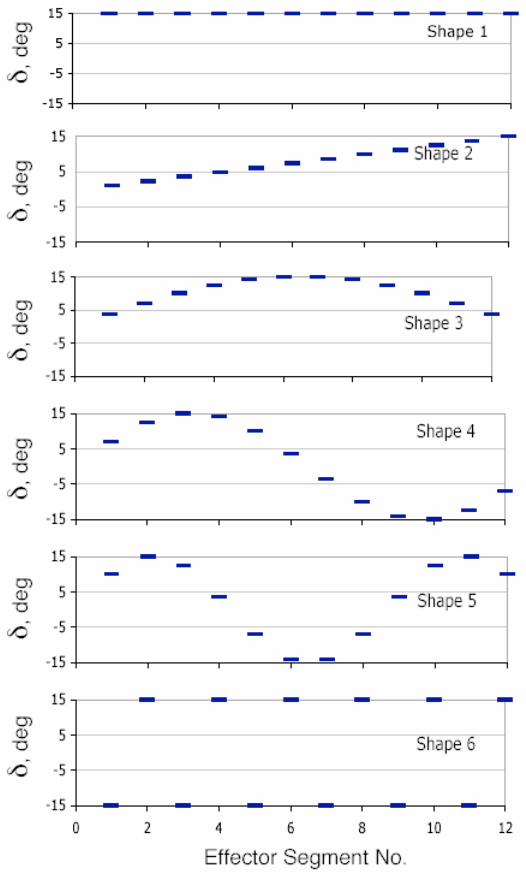

Figure 2.12: Effector deflection configurations tested on the MESA platform.[11]

Shape 1 resembles a conventional control surface and will serve as the basis for comparison for shapes 2 and 3. These two shapes are presumed to be lower-drag versions of conventional control surfaces. Shape 2 only exposes one end of the array to the flow, leaving the other end flush with the trailing edge of the wing. With only one distinct edge protruding into the flow, it is hoped that the induced drag caused by tip vortices will be reduced. Shape 3 takes this hypothesis one step further, placing both ends of the array flush with the wing's trailing edge, and thereby leaving no major perturbation in the flow. However, given that this discrete implementation of

a morphing wing is made from several individual control surfaces, tip vortices might be seen on each effector. The comparison of total drag produced by several small effectors in shapes 2 and 3 and drag produced by a single large control surface in shape 1 will be discussed later in this paper.

Shapes 4 and 6 are symmetric above and below the trailing edge of the wing; ideally, no pitch or lift will be created by these two shapes. A small amount of roll should be seen in shape 4 deflections due to the differing moment arms for each half of the effector array, but it should be practically negligible. Drag should be the only significant force produced by these two shapes. When tested one wing at a time, this drag should result in a yaw moment, but when both arrays are activated, only drag should be produced. Shape 5 is biased $\frac{2}{3}$ above and $\frac{1}{3}$ below the trailing edge in a positive deflection, so a small amount of lift and pitch is expected to be seen from these configurations. Drag, however, is expected to be the primary result of this configuration.

In addition to this type of analysis of the six array shapes, the data gathered from these tests[14] will be of use in the control prediction scheme to be created from the individual effector data. The results from the six shapes will serve as a reference comparison for the prediction scheme. It can reasonably be assumed that if the prediction scheme holds accurate over these array shapes, it will be accurate for virtually any possible configuration of the MESA effectors. If this is the case, then the database built from the individual effector tests would allow for very high amounts of customizability of desired aircraft response.

Chapter 3

Data Analysis

3.1 Baseline Aircraft

Baseline tests over α and β sweeps with no control surface deflections are graphed in Figure 3.1. The highlighted curve is the most detailed baseline test of the wind tunnel testing schedule. This figure shows very little dependence on sideslip angle for lift and pitching moments. The aircraft shows a gentle stall near an angle of attack of 19°. This type of gradual stall is typical of BWB aircraft. The lift curve slope for this aircraft is a relatively low 0.0617 deg^{-1}, or 3.54 rad^{-1}. Inviscid analysis[10] using the flow solver CMARC (Panel Method, Ames Research Center) predicted a lift curve slope for the *Thunderstruck* UAV of 3.64 rad^{-1}, closely resembling that found for the slightly modified MESA platform.

The pitching moment curve shows a period of static instability between angles of attack of 10° and 16°. This unstable region has been previously noted during flight-

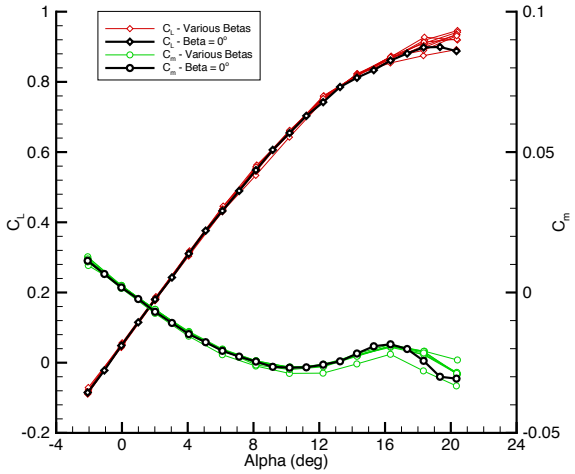

Figure 3.1: Pitching moment and lift curves for baseline MESA platform.

testing of the *Thunderstruck* UAV[15]. The aircraft trims for approach and landing at approximately $8\,^\circ - 10\,^\circ$, which is just at the beginning of the unstable region. The linear region of the pitching moment curve, which was taken to be from $-2\,^\circ$ to $+6\,^\circ$, varies from its CMARC prediction by a sizable 25% error, with an actual value of -0.248 rad^{-1} versus the CFD solution of -0.309 rad^{-1}.

3.2 Conventional Control Surfaces

The results of the anti-symmetric aileron sweeps are shown in Figure 3.2. Very little dependence on angle of attack is seen in the roll authority of the ailerons, which was found to be $-7.04 * 10^{-4}$ deg^{-1} at zero angle of attack. The power of these control surfaces was reduced from the designed control powers[10] because the ailerons were shortened significantly in the installation of the MESA effectors. Symmetric rudders are plotted in Figure 3.3, and symmetric elevons in Figure 3.4. A slight amount of

roll ($-9.97 * 10^{-5}\ deg^{-1}$) is seen with the rudder deflections to go along with its two primary authorities of yaw C_n ($4.31 * 10^{-4}\ deg^{-1}$) and side force C_Y ($-1.88 * 10^{-3}\ deg^{-1}$). The rudders for *Thunderstruck* were designed to be unnecessarily powerful in yaw, with a designed $\frac{d\beta}{d\delta_r}$ of 0.717[10].

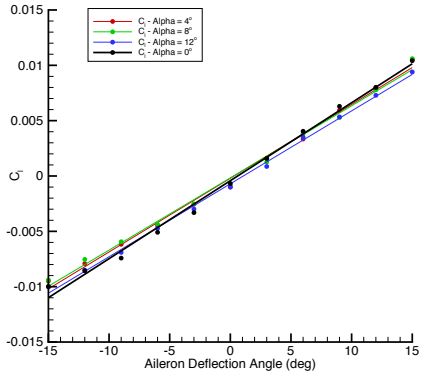

Figure 3.2: Rolling moment coefficient for anti-symmetric aileron deflections over an α range of $0\,^\circ$ to $+12\,^\circ$ with emphasis on the $0\,^\circ$ case.

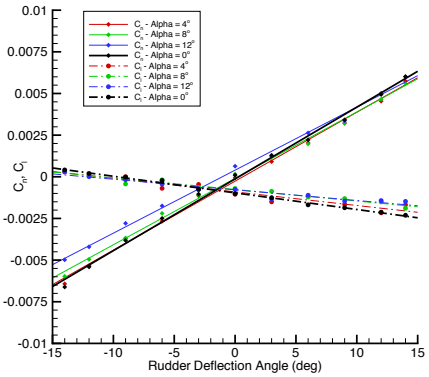

Figure 3.3: Yawing and rolling moment coefficients for rudder deflections.

The symmetric elevons show some variation in lift coefficient over the α range, but a large portion of this can be attributed to the small magnitudes of lift generated and limitations with the force balance. At high positive elevon deflections, α dependence is again seen. The variation from baseline grows larger with increasing angle of attack; this can easily be attributed to impinging stall or separation over the upper surface of the elevon at large deflections. The primary modes of effectiveness for the elevons are pitching moment and, to a lesser degree, lift, where their control powers at zero angle of attack are $-7.84 * 10^{-4}\ deg^{-1}$ and $2.95 * 10^{-3}\ deg^{-1}$, respectively. Symmetric aileron deflections were also tested (Figure 3.5). The primary control

authorities from these deflections are pitching moment, C_m, $(-9.59 * 10^{-4}\ deg^{-1})$ and lift, C_L, $(1.93 * 10^{-3}\ deg^{-1})$. The pitching moment shows little variation with angle of attack, but the lift coefficient shows a similar trend as what was seen with the elevon deflections. Once again, this can most likely be attributed to the small magnitudes of lift. A summary of the control authority of these four scenarios at zero angle of attack can be found in Table 6.1.

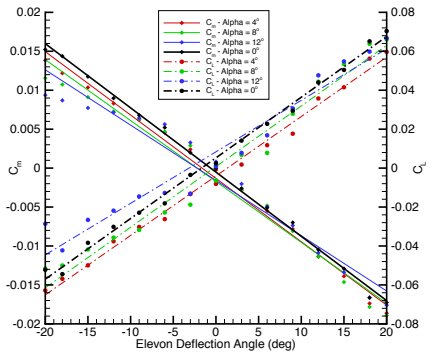

Figure 3.4: Pitching moment and lift coefficients for symmetric elevon deflections.

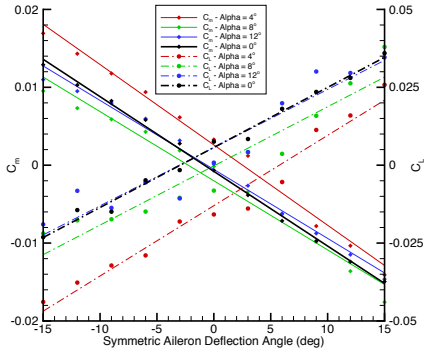

Figure 3.5: Pitching moment and lift coefficients for symmetric aileron deflections.

3.3 MESA Effectors

3.3.1 Individual Effectors

Each effector was run though a range of deflections from $-15\,^\circ$ to $+15\,^\circ$ at $\alpha's$ of $4\,^\circ$, $6\,^\circ$, and $8\,^\circ$. The pitching moment response to each effector deflection at an angle of attack of $4\,^\circ$ for the right and left wings are shown in Figure 3.6 and Figure 3.7, respectively. The average baseline run was subtracted off of each data point so to

return just the control power of the individual effector. All the effectors induce a similar response in aircraft pitching moment through their δ range. Table 6.2 lists the control powers for lift, pitch, and yaw for each effector on the right wing.

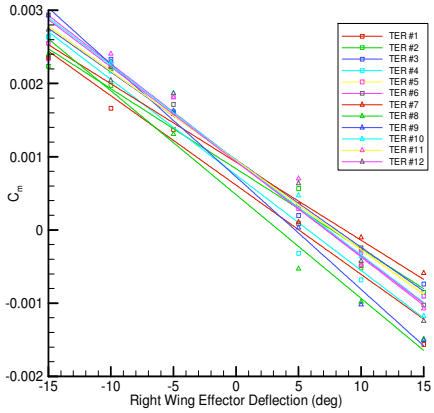

Figure 3.6: Pitching moment coefficients for right wing effectors at $\alpha = 4\,^{\circ}$.

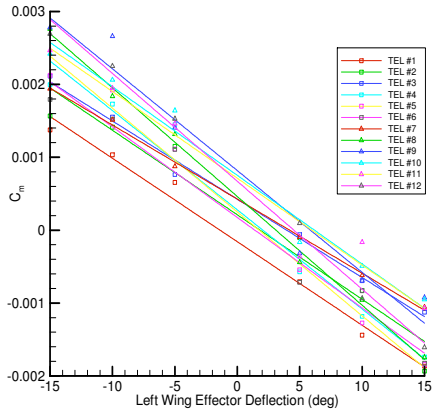

Figure 3.7: Pitching moment coefficients for left wing effectors at $\alpha = 4\,^{\circ}$.

Consistency is lacking across the effectors in lift control power; this is once again likely due to the small magnitudes of lift and the limitations of the force balance. Pitch and roll control show much more consistency across the effectors. Some of the variation in the pitching moment control powers can be attributed to the position of

the effectors with respect to the aircraft center of gravity. The first six effectors all lie on a line parallel to the aircraft's y-axis and should therefore show no significant variation in pitching moment, but the second set of effectors lies on the swept portion of the wing, which results in variable moment arms to the center of gravity. It is also of interest to note that effector #7 consistently shows control values lower than all other effectors. This effector is the first surface after the change in sweep of the wing. A small section of the trailing edge of this effector had to be cut away to allow it to move past effector #6. Thus, the surface area of this effector is reduced, and it is only logical that the control powers would also be lessened. Table 6.3 lists the same control powers for the left wing, and similar observations can easily be made.

3.3.2 Effector Shapes

Effector array shape 1 simulates a conventional control surface, and it can be directly correlated to a set of elevons (symmetric deflection) or ailerons (anti-symmetric deflection). Figure 3.8 shows the lift and pitching moment coefficient response to a symmetric shape 1 deflection. The rolling moment coefficient response to the anti-symmetric shape 1 deflection is shown in Figure 3.9.

Figure 3.10 and Figure 3.11 show the same attributes of the model to a shape 2 deflection, as do Figures 3.12 and 3.13 for a shape 3 stimulus. Clearly, shape 1 is the most powerful of the three for commanding pitch or roll changes. However, it could also be beneficial to examine the drag production of each of these shapes. Intuitively, one would assume that shape 1 would produce the most drag of the three shapes due to its distinct tips at the edge of the array surface. Shape 2 only has one exposed tip to induce drag, and shape 3 has none. Indeed, Figures 3.14 through 3.17 show that

shape 1 produces significantly more drag than either shape 2 or 3 in both symmetric and anti-symmetric configurations. Figure 3.18 and Figure 3.19 compare shapes 2 and 3 and show very similar drag characteristics from both configurations.

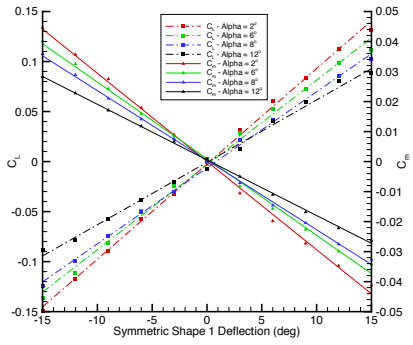

Figure 3.8: Pitching moment and lift curves for symmetric shape 1 deflections for an α range of $+2^\circ$ to $+12^\circ$.

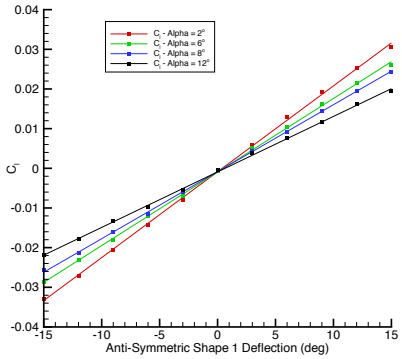

Figure 3.9: Rolling moment curves for anti-symmetric shape 1 deflections for an α range of $+2^\circ$ to $+12^\circ$.

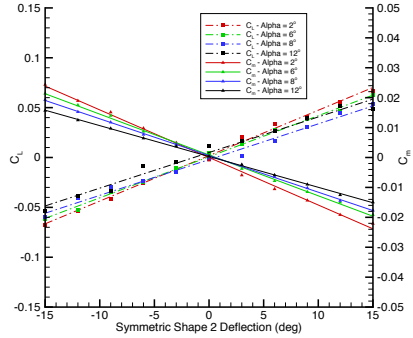

Figure 3.10: Pitching moment and lift curves for symmetric shape 2.

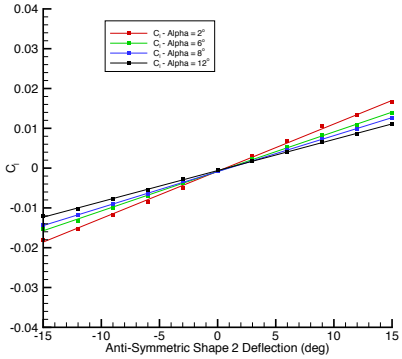

Figure 3.11: Rolling moment curves for antisymmetric shape 2.

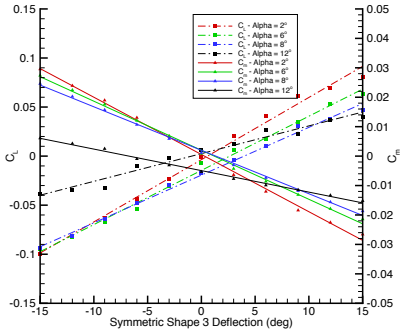

Figure 3.12: Pitching moment and lift curves for symmetric shape 3.

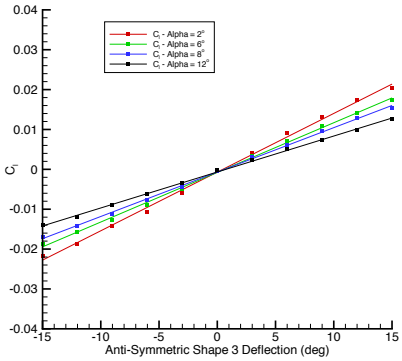

Figure 3.13: Rolling moment curves for anti-symmetric shape 3.

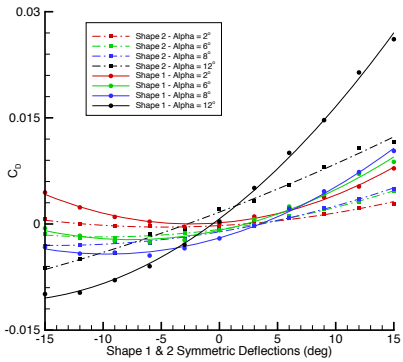

Figure 3.14: Drag coefficient comparison for symmetric shapes 1 and 2.

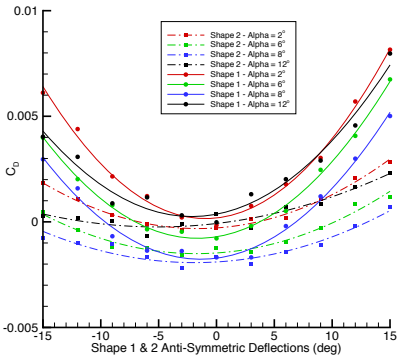

Figure 3.15: Drag coefficient comparison for anti-symmetric shapes 1 and 2.

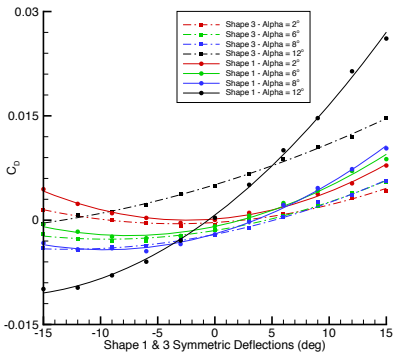

Figure 3.16: Drag coefficient comparison for symmetric shapes 1 and 3.

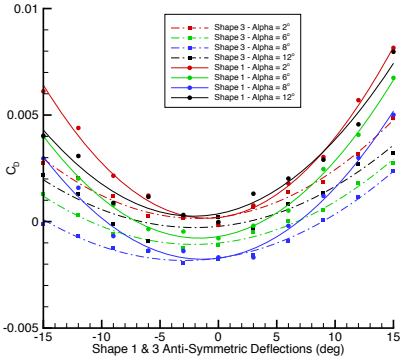

Figure 3.17: Drag coefficient comparison for anti-symmetric shapes 1 and 3.

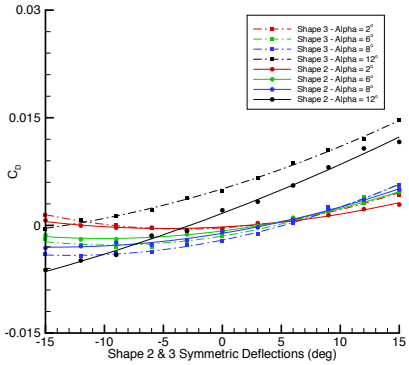

Figure 3.18: Drag coefficient comparison for symmetric shapes 2 and 3.

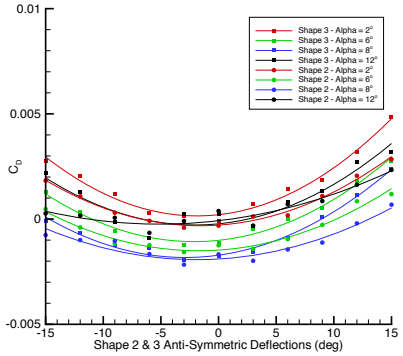

Figure 3.19: Drag coefficient comparison for anti-symmetric shapes 2 and 3.

Knowing that shapes 2 and 3 produce less drag than shape 1 but also have less authority, it is desired to discover which is more efficient. Figure 3.20 displays lift to drag ratio for the entire aircraft for shapes 1, 2, and 3 for an α of $+6\,^{\circ}$. All three configurations have very similar lift to drag ratios over the positive deflection range, but for high negative deflections, shape 1 has a considerable lower ratio than the others.

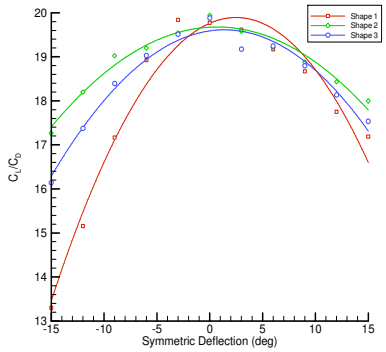

Figure 3.20: Lift to drag ratio for shapes 1, 2, and 3 at $\alpha = +6\,^{\circ}$.

Figure 3.21 shows rolling moment to drag ratio. Surprisingly, shape 1 is the most efficient of the three, opposite of the expectations of the results. Figure 3.22 shows a similar trend for pitching moment to drag ratio. This could be due to the limitations imposed by the discretized approximation of a continuously morphing trailing edge. Each effector can create trailing tip vortices. On an ideally manufactured continuously morphing trailing edge, there would be no singularities or breaks to disrupt the flow and create drag. Additionally, the sides of the MESA effectors are hollow, allowing for the possibility of air entering through the sides and creating drag from the inside surfaces of the effector. One interesting point that can be made on both Figures 3.21 and 3.22 is that the intersection and inflection points of the curves occur at a non-zero value on the y-axis. These values are due to the non-zero values for

drag, roll, and pitch from the wind-tunnel data. The baseline aircraft data were subtracted from the data collected during deflected control surface runs, but the baseline runs did not necessarily match up perfectly with the zero-deflection runs. This is due to simple wind-tunnel errors such as air turbulence. Along the x-axis, these points lie at deflections of 0°, as would be intuitively expected.

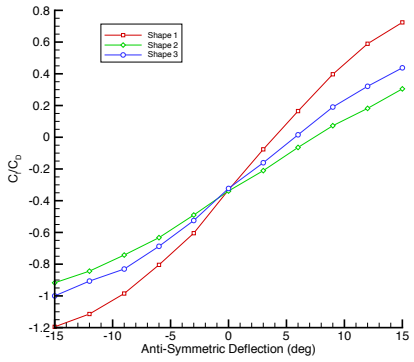

Figure 3.21: Rolling moment to drag ratio for anti-symmetric shapes 1, 2, and 3.

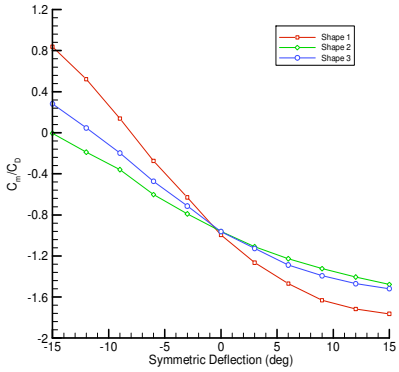

Figure 3.22: Pitching moment to drag ratio for symmetric shapes 1, 2, and 3.

When compared to the conventional control surfaces, shape 1 is seen to create up to twice the authority in pitch and lift as the existing elevons, while shapes 2 and 3 are very similar to the elevons. The large advantage that shape 1 holds can easily be attributed to the size of the effector arrays, which are approximately twice as large as the elevons. The conventional ailerons are generally overpowered by the MESA effectors in all three shapes, despite the advantage that the ailerons hold in having a longer moment arm. However, during the construction of the MESA effectors, the existing ailerons on the *Thunderstruck* UAV were cut in size by half. Therefore, the roll control authority designed for the original aircraft would be approximately double what was seen in the aileron tests on the MESA platform. Given this information,

it is seen that the existing MESA array can perform the job of the original ailerons for shapes 1, 2, and 3. If more roll control was needed, the array could be extended farther toward the tip of the wing.

Shapes 4, 5, and 6 were initially believed to be useful only for drag and yawing purposes. Figures 3.23 and 3.24 show the drag coefficients for these shapes at an angle of attack of $+6\,^{\circ}$. Note that each plot only displays one side of the aircraft; in order to calculate drag values that would be obtained for deflections applied to both sides of the aircraft, the values of these two figures should be summed. Referring back to the drag values shown for shapes 1, 2, and 3 in Figures 3.14 through 3.19, it is clear that shape 6 creates considerably higher drag than any other configuration.

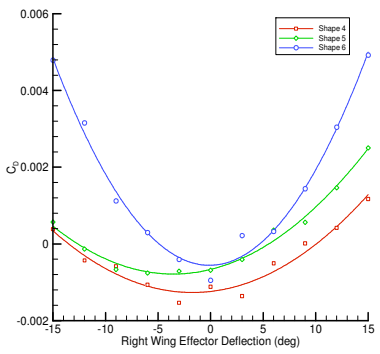

Figure 3.23: Drag coefficients for right wing effectors for shapes 4, 5, and 6.

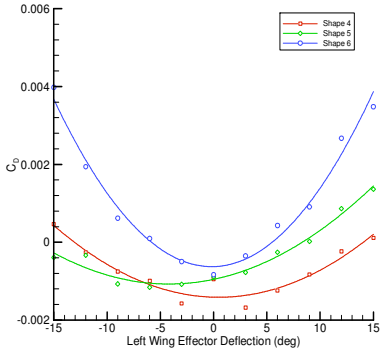

Figure 3.24: Drag coefficients for left wing effectors for shapes 4, 5, and 6.

Figures 3.25 and 3.26 translate these single-sided drag forces into yawing moments. Shape 6 shows that a significant moment was created, but it is not as high as the moments generated by the rudders (Figure 3.3). A $15\,^{\circ}$ rudder deflection creates up to five times as much yaw authority as a $15\,^{\circ}$ shape 6 deflection. With the current configuration, the MESA array is not powerful enough to completely supplant the

rudder in yaw control. Perhaps a larger array or a similar array placed farther outboard on the wings could create a yawing moment high enough to be capable of entirely replacing the rudder, which, as previously mentioned, was designed to be overly powerful. If the array was to be used in this manner, the moment arm to the 12-unit array would have to be more than doubled or more than twice the effectiveness would have to be created at the existing moment arm. However, one minor advantage that can be pointed out for the use of drag rudders is the lack of induced roll that is present in rudder deflections.

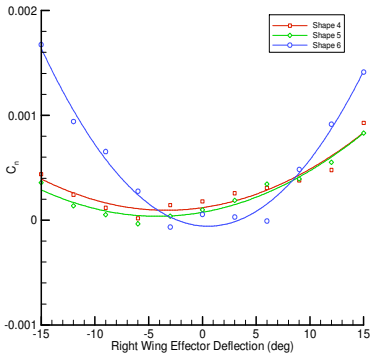

Figure 3.25: Yawing moment coefficients for right wing effectors for shapes 4, 5, and 6.

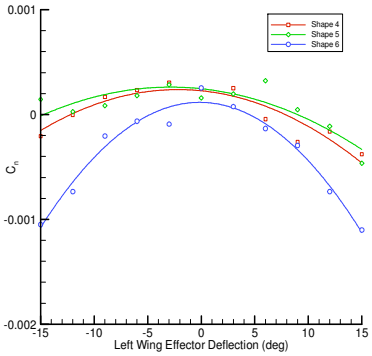

Figure 3.26: Yawing moment coefficients for left wing effectors for shapes 4, 5, and 6.

Lift, pitching moment, and rolling moment coefficients (Figures 3.27 through 3.30) are almost negligible for these configurations when compared to shapes 1, 2, and 3 (Figures 3.8 through 3.13). It has previously been shown[6] that the pressure distributions of these three shapes are relatively flat, so it would logically follow that very little lift, pitch, or roll would be created.

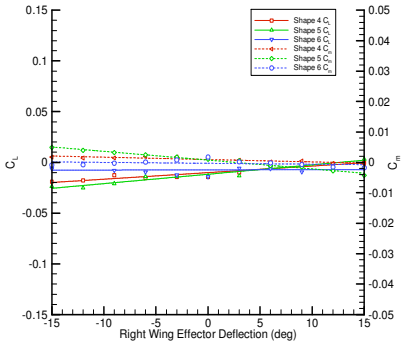

Figure 3.27: Pitching moment and lift coefficients for right wing effectors for shapes 4, 5, and 6.

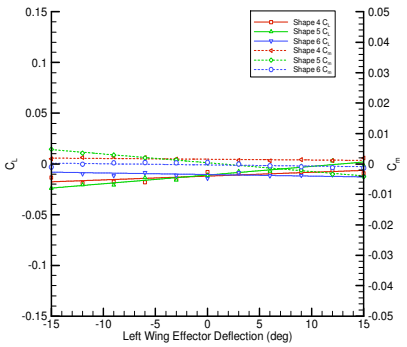

Figure 3.28: Pitching moment and lift coefficients for left wing effectors for shapes 4, 5, and 6.

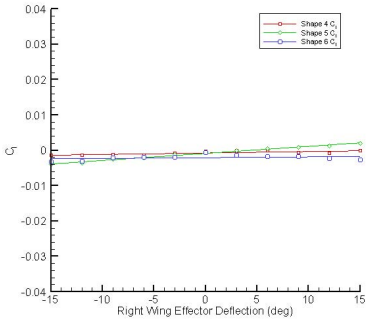

Figure 3.29: Rolling moment coefficients for right wing effectors for shapes 4, 5, and 6.

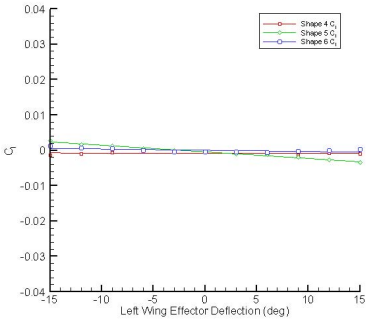

Figure 3.30: Rolling moment coefficients for left wing effectors for shapes 4, 5, and 6.

Chapter 4

Prediction Methods

Following the reduction of the previous data, it is of concern to devise a method to manipulate these values such that the control effectiveness can be found for any configuration of the MESA effectors. One such method for doing so is detailed below.

4.1 Lift, Pitch, and Roll

4.1.1 Angles of Attack of $+4^\circ$, $+6^\circ$, and $+8^\circ$

For each data point in the single effector runs, the force generated by the effector is defined as the difference between the total aircraft force and the aircraft baseline force:

$$C_{X_{Effector}} = \Delta C_X = C_{X_{Measured}} - C_{X_{Baseline}} \tag{4.1}$$

Where C_X is any of the six basic control parameters, $C_{X_{Measured}}$ is the force generated by the entire aircraft with a control surface deflection as read from the force balance in the wind tunnel, and $C_{X_{Baseline}}$ is the average of the three runs previously defined as baseline runs. Due to the amount of noise in the wind tunnel, each baseline run differed slightly from the others, so it was thought best to average all the runs as a means of error reduction.

From each of these data values, the control powers for each effector can be defined as

$$C_{X_{\delta_f}} = \frac{\partial C_X}{\partial \delta_f} \tag{4.2}$$

The lift, pitch, and roll control powers were approximated as linear variations for the control surface deflections tested. As seen previously (Figures 3.6 and 3.7), this approximation is very acceptable, as would be expected at low angles of attack with small deflections. The control powers generated from the single effector runs are detailed in Tables 6.2 and 6.3. For any given effector and deflection, it is known how to find the resultant control authority:

$$C_X = C_{X_{\delta_f}} \delta_f = \frac{\partial C_X}{\partial \delta_f} \delta_f \tag{4.3}$$

Expanding this to n flaps can be achieved with a simple summation:

$$C_{X_{total}} = \sum_{i=1}^{n} C_{X_{\delta_f,i}} \delta_{f,i} \tag{4.4}$$

Thus, the lift, pitch, and roll authorities can be found for any configuration of the MESA effectors, given that the aircraft operating angle of attack is chosen from the three $\alpha's$ tested in the wind tunnel.

Appendix A shows this technique applied to all six shapes at angles of attack of $+4\,^{\circ}$, $+6\,^{\circ}$, and $+8\,^{\circ}$. It is clear that the predictions for each configuration's primary mode of effectiveness are very good. Pitching moment and lift are very accurately modeled for symmetric shape 1, 2, and 3 configurations. Rolling moment is accurately predicted for anti-symmetric deflections of these three shapes. Predictions for non-primary modes of effectiveness leave much more room for improvement, however. The only prediction that shows significant error is lift for the anti-symmetric deflections for shapes 1, 2, and 3. The predicted values for lift are typically very small, as would be expected since a positive deflection on one wing should essentially cancel out a negative deflection on the other wing, with the only difference coming in points of flow separation. However, the experimental results show that the two do not completely negate each other. The lift generated by these configurations is very inconsistent across the deflection range. Still, even though the percentage error may be very large on these predictions, the magnitude of error is small compared that of the entire aircraft or a full control surface deflection.

For shapes 4, 5, and 6, the simple prediction scheme once again shows fair accuracy in all components except for lift. Shapes 4 and 6 would intuitively produce close to zero lift, but these results were once again very inconsistent in the wind tunnel results. Shape 5 deflections show more regularity in the trend for lift, but there is

still a significant percentage error for the predicted values for lift.

An obvious source of error lies in the determination of the control power for the effectors. Each effector creates a very small change in aircraft aerodynamics, and small disturbances in the force balance and data collection systems could contribute significantly to error in control authority. Even so, the method described above is shown to be very accurate for primary coefficient prediction at the three tested angles of attack.

4.1.2 All Other Angles of Attack

The above method has only been developed to draw from the database of experimentally tested angles of attack. For use in a wider range of flight conditions, however, a slightly more advanced method of prediction must be formulated. Given the results of the baseline tests of the aircraft (Figure 3.1) and effectors (Figures 3.6 and 3.7, for example), as well as the acceptable results from the method outlined above, it is clear that linear relationships can be established across a range of low angles of attack.

Equation 4.2 can be used as the basis for a similar parameter, defined with the addition of an angle of attack component:

$$C_{X_{\delta_f}\alpha} = \frac{\partial C_{X_{\delta_f}}}{\partial \alpha} = \frac{\partial^2 C_X}{\partial \alpha \, \partial \delta_f} \tag{4.5}$$

All linear data for the three tested angles of attack can be found in Tables 6.4 and 6.5. Equation 4.5 can now be applied to find the resulting control authority for lift, pitch, and roll using the following:

$$C_X = C_{X_{\delta_f \alpha}} \delta_f \alpha = \frac{\partial^2 C_X}{\partial \alpha \, \partial \delta_f} \delta_f \alpha \tag{4.6}$$

Similar to Equation 4.4, this can be expanded to n flaps with a summation:

$$C_{X_{total}} = \alpha \sum_{i=1}^{n} C_{X_{\delta_f \alpha, i}} \delta_{f,i} \tag{4.7}$$

When using this method, it would be predicted that the accuracy would be diminished at the three experimental angles of attack. The results show that this method is indeed less accurate at these three angles of attack. Nevertheless, this method provides a way to study the effects of the MESA array at a variety of other angles of attack within the linear regime.

4.2 Drag and Yaw

4.2.1 Second Degree Polynomial Scheme

The above approach should not be applied to drag or yaw due to the parabolic nature of both of these parameters. High deflections in both the positive and negative directions for each effector should produce high amounts of drag, while small deflections should produce low amounts of drag, resulting in a parabolically shaped drag bucket. An exception to this expectation might be surmised at high negative deflections at high positive angles of attack. This configuration effectively reduces the frontal area of the aircraft and could result in a net decrease in drag. Nevertheless, a system different from the previously shown linear system must be created for

predicting drag and yaw. Upon closer examination of the available data, however, it is clear that the limitations of the force balance in the wind tunnel have severely impacted the accuracy of the data for both drag and yaw. For example, Figure 4.1 shows the measured values of drag for left wing effectors 10 and 11. These two effectors lie immediately next to each other, but the difference in the measured values is unexplainable by pure aerodynamics. However, the majority of data drawn from these tests is reasonable.

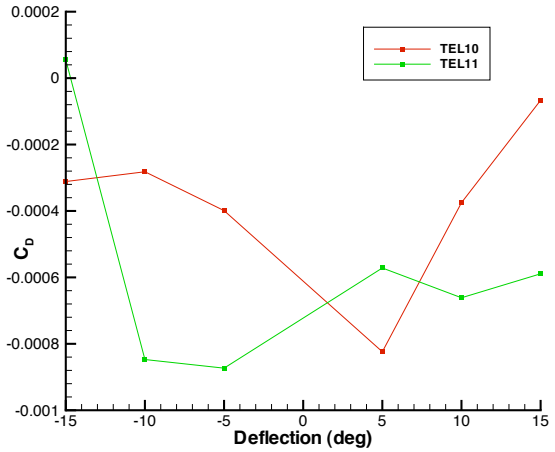

Figure 4.1: Comparison of drag for left wing effectors 10 and 11 at $\alpha = 4\,^{\circ}$

Despite the occasional strange effector data, a prediction method was attempted for drag. The general scheme should logically be very similar to that used for lift, pitch, and roll. For each effector, a second-order polynomial curve fit was applied to the recorded data, resulting in a non-linear control authority:

$$C_D = A{\delta_f}^2 + B\delta_f \tag{4.8}$$

where A and B are the polynomial curve constants.

In a similar fashion to Equation 4.4, the total drag values should be able to be calculated using the following equation:

$$C_{D_{total}} = \sum_{i=1}^{n} \left[A_i \delta_{f,i}^2 + B_i \delta_{f,i} \right] \tag{4.9}$$

Appendix B shows the results of this method applied to all six shapes at the three standard angles of attack. Shape 6 shows the best correlation between the prediction and the wind-tunnel results. Anti-symmetric shapes 1, 2, and 3 show massive amounts of error, but all other configurations are much closer. Proper trends exist for all other configurations, but a significant amount of offset error is present for most cases.

In an attempt to create a more accurate method for predicting drag, one can examine the yaw values. It is mathematically feasible to attempt to withdraw the drag values from the yaw values for each effector, knowing that drag is the only contributor to yaw in these wind tunnel tests. With the limitations of the force balance taken into consideration, it could be hypothesized that the yaw values might be more accurate than merely the drag values, as yaw is generated from drag occurring some distance away from the balance center. The small drag values are multiplied by the moment arm of each effector to produce a yawing moment, essentially magnifying the drag forces into those which would hopefully be readable by the force balance. Therefore, each effector's yaw value can be converted to a drag value using:

$$C_D = \frac{b}{y} C_n \tag{4.10}$$

where y is the spanwise distance from the centerline of the aircraft to the center of

the control surface. After these new drag values have been found for each effector, the method shown in Equations 4.8 and 4.9 can be attempted again. Appendix C shows the results of this method as applied to shapes 4, 5, and 6. Unfortunately, this method supplies predictions significantly worse than the original method.

The method shown in Equations 4.8 and 4.9 was also applied to the yaw data. Appendix B contains the results of the predictions for yaw for all six shapes. The predictions occasionally mimic the experimental data, but the overwhelming majority of these cases resulted in unacceptable results.

4.2.2 Gauss Interpolation Scheme

A Gauss interpolation method was performed on the drag data in another effort to create a legitimate prediction scheme. The Gauss interpolation was performed on each effector for the array configuration using the following equation:

$$\begin{aligned} C_D &= \frac{(\delta_f - \delta_{f,1})(\alpha - \alpha_1)C_{D,22} + (\delta_f - \delta_{f,1})(\alpha_2 - \alpha)C_{D,21}}{(\delta_{f,2} - \delta_{f,1})(\alpha_2 - \alpha_1)} \\ &+ \frac{(\delta_{f,2} - \delta_f)(\alpha - \alpha_1)C_{D,12} + (\delta_{f,2} - \delta_f)(\alpha_2 - \alpha)C_{D,11}}{(\delta_{f,2} - \delta_{f,1})(\alpha_2 - \alpha_1)} \end{aligned} \tag{4.11}$$

Where C_D is the value at the desired α and δ_f, and the subscripts 1 and 2 denote the experimental datum points immediately above and below the prescribed angle of attack and deflection angle. Using this method should result in more accurate prediction data for drag for each effector, as this scheme is an interpolation between existing data points. This scheme should also be useful in solving the inverse problem of aircraft control, where a control algorithm selects the proper effector configuration

based on user-prescribed values for drag.

When applied to the experimental drag values, however, this method breaks down. The interpolation resulted in most drag values being negative, as the original data was extremely noisy. When the baseline aircraft data was subtracted from the effector deflection data, a majority of the drag values came out negative. This can once again be explained by the limitations of the force balance. Each effector creates an extremely small amount of drag, and in a wind tunnel with high amounts of turbulence, such as the LaRC 12-foot, these drag values can easily be within the limits of data variation due to turbulence effects on the aircraft.

Chapter 5

Concluding Remarks

5.1 Summary of Results

This study examines the control effectiveness of a distributed actuation system on a blended-wing-body UAV using results from six weeks of wind-tunnel testing in the 12-foot subsonic tunnel at NASA's Langley Research Center. The results from the tests were used to create a method by which the control parameters can be predicted for any configuration of the effector array.

The distributed actuation system is implemented on a BWB UAV created at NC State University. The UAV has a wingspan of 9.38 ft with root and tip chords of 58 in and 5.25 in. The effector array was implemented 25 in from the centerline of the aircraft and extended for 18 in on each wing. Each effector was created from two pieces of spring steel, with dimensions of 0.007 in (thickness), 1.5 in (width), and 4 in (length), set in a pull-pull configuration with a standard hobbyist's nano-

servo. Twelve independently actuated effectors were placed on each wing. Directly upstream from each effector, pressure taps were installed, though no data from them were used in this analysis.

The wind-tunnel tests performed on this vehicle encompassed a wide array of baseline, conventional control surface, and MESA tests. Initial tests were performed across a wide range of angles of attack and sideslip with no control surface deflections. Following these, tests were then performed on the conventional control surfaces remaining on the UAV: rudders, elevons, and ailerons. After recording data from these tests, the effector array was tested in a variety of configurations. The first set of tests recorded forces and moments generated by each individual effector of a range of deflections of $\pm 15^\circ$ at angles of attack of 4°, 6°, and 8°. After data had been gathered from each effector, the arrays were configured into a variety of shapes, all of which were tested over the same deflection and angle of attack range. The six shapes tested were a constant offset, linear offset, sine waves of one half, one, and one and a half periods, and a one-up, one-down, zig-zag shape. All six of these shapes were compared to the results from the conventional control surfaces. Shapes 1, 2, and 3 were shown to be sufficient enough in lift, pitch, and roll to completely replace the ailerons and elevons. Shapes 4, 5, and 6 were found to be less than half as effective as the conventional rudders at producing yaw, but the current implementation suggests that a larger array of effectors could produce adequate amounts of yaw control using shape 6 deflections.

A method is described that uses the data from testing each individual effector to predict the control powers for any configuration of the array. The predictions for lift, pitch, and roll have a high degree of accuracy within the linear range of angles

of attack. Drag and yaw predictions were much more erroneous, probably due to the limitations of the force balance and the extremely small amounts of drag created by the individual effectors. The prediction scheme for lift, pitch, and roll incorporates simple addition of the linear control powers for each effector. The scheme for drag and yaw is only slightly more complex, using a second-order polynomial control power for each effector. A Gauss interpolation scheme was also attemped for drag values, but it also broke down under the limitations of the force balance and the amount of turbulence in the LaRC 12-Foot Wind Tunnel.

5.2 Recommendations for Future Work

Research into the general field of morphing aircraft is still in its early stages, and many projects are still in their research phases. The databases created in this project could be utilized in a closed-loop controller for test flights of the MESA platform. The response time and control powers of the MESA effectors exhibited in this paper show that this aircraft is a candidate for test flights. If future versions of the MESA testbed are to be built, it would be suggested that the array be much larger to allow for the possibility of flight without rudders or vertical tails. Also, the addition of a second pressure tap on the bottom of each effector could allow for a blending of desired lift characteristics and spanwise pressure distributions for optimization of multiple design criteria.

Chapter 6

Tables

Table 6.1: Control powers for conventional control surfaces (deg^{-1}).

	$C_{L_{\delta_f}} * 10^4$	$C_{m_{\delta_f}} * 10^4$	$C_{l_{\delta_f}} * 10^4$	$C_{n_{\delta_f}} * 10^4$	$C_{Y_{\delta_f}} * 10^4$
Anti-Symmetric Ailerons	-1.423	1.377	7.044	0.00192	0.5418
Rudders	1.599	-0.5097	-0.9966	4.306	-18.80
Elevons	31.15	-8.248	0.2099	0.01871	0.3398
Symmetric Ailerons	19.28	-9.591	-1.229	-0.1597	-0.3975

Table 6.2: Lift, pitch, and roll control powers for right wing effectors (deg^{-1}).

	$\alpha = 4^\circ$			$\alpha = 6^\circ$			$\alpha = 8^\circ$		
Effector	$C_{L_{\delta_f}}$	$C_{m_{\delta_f}}$	$C_{l_{\delta_f}}$	$C_{L_{\delta_f}}$	$C_{m_{\delta_f}}$	$C_{l_{\delta_f}}$	$C_{L_{\delta_f}}$	$C_{m_{\delta_f}}$	$C_{l_{\delta_f}}$
1	5.416	-1.220	0.8950	5.450	-1.435	0.7531	6.494	-1.360	0.8043
2	4.425	-1.092	0.9735	3.943	-1.047	0.7667	3.546	-1.089	0.7207
3	5.020	-1.196	0.9896	4.409	-1.146	0.8169	2.828	-1.222	0.7861
4	3.883	-1.304	0.8463	4.063	-1.114	0.9491	6.440	-1.201	0.9639
5	4.232	-1.218	0.9740	5.079	-1.275	0.8401	5.502	-1.297	0.9227
6	3.449	-1.320	1.069	4.386	-1.440	1.092	1.827	-1.110	0.8114
7	2.661	-1.068	0.7600	2.269	-1.003	0.8661	3.358	-0.9067	0.6929
8	3.573	-1.418	1.094	3.297	-1.309	1.133	4.600	-1.306	1.082
9	3.665	-1.538	0.9499	2.133	-1.349	0.9147	3.717	-1.113	0.9275
10	2.711	-1.296	1.126	4.343	-1.174	1.013	4.415	-1.152	0.7197
11	3.859	-1.220	0.8807	3.221	-1.286	0.9260	1.288	-0.8181	0.6380
12	3.479	-1.292	0.9356	2.795	-1.091	0.8121	2.441	-0.9957	0.7725

All values $*10^{-4}$

Table 6.3: Lift, pitch, and roll control powers for left wing effectors (deg^{-1}).

	$\alpha = 4^\circ$			$\alpha = 6^\circ$			$\alpha = 8^\circ$		
Effector	$C_{L_{\delta_f}}$	$C_{m_{\delta_f}}$	$C_{l_{\delta_f}}$	$C_{L_{\delta_f}}$	$C_{m_{\delta_f}}$	$C_{l_{\delta_f}}$	$C_{L_{\delta_f}}$	$C_{m_{\delta_f}}$	$C_{l_{\delta_f}}$
1	3.805	-1.145	-0.7703	5.587	-1.219	-0.6466	4.793	-1.191	-0.8078
2	5.285	-1.159	-0.7455	4.076	-1.222	-0.6429	4.133	-1.249	-0.7312
3	3.988	-1.073	-0.8779	2.742	-1.169	-0.8866	5.321	-1.313	-0.8897
4	5.147	-1.361	-0.9126	3.015	-1.100	-0.9136	4.772	-1.277	-0.8272
5	3.579	-1.425	-0.8842	5.692	-1.294	-0.8262	4.209	-1.232	-0.9663
6	5.428	-1.242	-0.7816	2.938	-1.223	-0.9099	6.856	-1.293	-0.7911
7	3.698	-1.016	-0.8047	3.369	-1.136	-0.7502	1.788	-0.8133	-0.6053
8	4.946	-1.491	-1.000	2.564	-1.157	-0.9833	2.950	-1.148	-0.8690
9	6.282	-1.396	-0.9063	3.567	-1.243	-0.9479	2.078	-0.9065	-0.7065
10	3.340	-1.216	-0.9281	2.692	-1.225	-0.9944	2.994	-0.8476	-0.7917
11	3.285	-1.190	-0.9173	4.363	-1.119	-0.8944	1.013	-0.8564	-0.7058
12	4.473	-1.479	-0.9436	3.439	-1.233	-0.8852	0.9439	-1.024	-0.8362

All values $*10^{-4}$

Table 6.4: Linear curve fit data for right wing effectors with α variation.

	$C_{L_{\delta_f}\alpha}$			$C_{m_{\delta_f}\alpha}$			$C_{l_{\delta_f}\alpha}$		
Effector	Slope	Int.	r^2	Slope	Int.	r^2	Slope	Int.	r^2
1	2.695	4.170	0.7736	-0.3500	-1.128	0.4115	-0.2268	0.9535	0.3983
2	-2.198	5.290	0.9969	0.0075	-1.081	0.0036	-0.6320	1.200	0.8812
3	-5.480	7.374	0.9387	-0.0650	-1.149	0.1133	-0.5088	1.170	0.8605
4	6.393	0.9598	0.8025	0.2575	-1.361	0.2932	0.2940	0.7434	0.8427
5	3.175	3.033	0.9642	-0.1975	-1.145	0.9386	-0.1283	0.9892	0.1442
6	-4.055	5.654	0.3924	0.5250	-1.605	0.3952	-0.6440	1.377	0.6835
7	1.743	1.717	0.3992	0.4033	-1.235	0.9876	-0.1678	0.8737	0.1476
8	2.568	2.283	0.5593	0.2800	-1.512	0.7701	-0.0300	1.121	0.0506
9	0.1300	3.094	0.0008	1.063	-1.971	0.9959	-0.0560	0.9643	0.3952
10	4.260	1.267	0.7816	0.3600	-1.423	0.8615	-1.016	1.562	0.9384
11	-6.428	6.646	0.9220	1.005	-1.711	0.6296	-0.6068	1.179	0.6140
12	-2.595	4.462	0.9674	0.7408	-1.571	0.9593	-0.4078	1.085	0.9189

Slope values $*10^{-5}$

Intercept values $*10^{-4}$

Table 6.5: Linear curve fit data for left wing effectors with α variation.

	$C_{L_{\delta_f}\alpha}$			$C_{m_{\delta_f}\alpha}$			$C_{l_{\delta_f}\alpha}$		
Effector	Slope	Int.	r^2	Slope	Int.	r^2	Slope	Int.	r^2
1	2.470	3.246	0.3062	-0.1150	-1.116	0.3789	-0.0937	-0.6853	0.0494
2	-2.880	6.226	0.7130	-0.2250	-1.075	0.9494	0.0358	-0.7280	0.0166
3	3.333	2.018	0.2671	-0.6000	-0.8250	0.9868	-0.0295	-0.8670	0.9302
4	-0.9375	4.874	0.0271	0.2100	-1.372	0.0994	0.2135	-1.013	0.7412
5	1.575	3.548	0.0843	0.4825	-1.607	0.9591	-0.2053	-0.7691	0.3401
6	3.570	2.932	0.1297	-0.1275	-1.176	0.4962	-0.0238	-0.8133	0.0044
7	-4.775	5.817	0.8747	0.5068	-1.293	0.3861	0.4985	-1.019	0.9359
8	-4.990	6.481	0.6094	0.8575	-1.780	0.7697	0.3275	-1.147	0.8439
9	-10.51	10.28	0.9724	1.224	-1.916	0.9553	0.4995	-1.153	0.5993
10	-0.8650	3.528	0.2847	0.9210	-1.649	0.7317	0.3410	-1.109	0.4355
11	-5.680	6.295	0.4413	0.8340	-1.556	0.9009	0.5288	-1.156	0.8302
12	-8.823	8.246	0.9460	1.138	-1.928	0.9978	0.2685	-1.049	0.9975

Slope values $*10^{-5}$

Intercept values $*10^{-4}$

Bibliography

[1] McGowan, A., Cox, D., Lazos, B., Waszak, M., Raney, D., Siochi, E., Pao, S. P., "Biologically-Inspired Technologies in NASA's Morphing Project," Proceedings of SPIE Vol. 5051, 2003.

[2] Gano, S., Renaud, J., "Optimized Unmanned Aerial Vehicle with Wing Morphing for Extended Range and Endurance," AIAA Paper 2002-5668, 2002.

[3] Gano, S. E., Renaud, J. E., Batill, S. M., Tovar, A. "Shape Optimiaztion for Conforming Airfoils," AIAA Paper 2003-1579, 2003.

[4] Roth, B., Crossley, W., "Application of Optimization Techniques in the Conceptual Design of Morphing Aircraft," AIAA Paper 2003-6733, 2003.

[5] Kudva, J. N., Martin, C. A., Scherer, L. B., Jardine, A. P., McGowan, A. R., Lake, R. C., Sendeckyj, G., Sanders, B., "Overview of the DARPA/AFRL/NASA Smart Wing Program," Part of the SPIE Conference on Industrial and Commerical Applications of Smart Structures Technologies, SPIE Vol. 3674, 1999.

[6] Barnwell, W. G., *Distributed Actuation and Sensing on an Unihabited Aerial Vehicle,* Master's Thesis, North Carolina State University, August 2003.

[7] Kudva, J. N., "Overview of the DARPA Smart Wing Project," Journal of Intelligent Material Systems and Structures, Vol. 15, No. 4, 2004.

[8] Kudva, J. N., Garcia, E., Pinkerton-Florance, J. L., Sanders, B. P., "Overview of the DARPA/AFRL/NASA Smart Wing Phase II Program," Proceedings of SPIE Vol. 4332, 2001.

[9] Liebeck, R.H.; Page, M.A., "Evolution of the Revolutionary Blended-Wing-Body," NASA Center for Aerospace Information, 1996.

[10] "UAV *Thunderstruck:* Fall Report", NC State University Senior Aircraft Design Class: Fall Report, December 2001.

[11] Raney, D. L., Cabell, R. H., "Wind Tunnel Test of an RPV with Shape-Change Control Effector and Sensor Arrays," AIAA paper 2004-5114, August 2004.

[12] King, R. M., *On the Use of Wing Adaptation and Formation Flight for Improved Aerodynamic Efficiency,* Doctorate Dissertation, North Carolina State University, 2005.

[13] Lee, J. D., Janiszewska, J. M., "A Simple Method for Determining Lift and Drag on a Wing," AIAA paper 2005-1061, 2005.

[14] Lion, S. Todd, Static Force Tests in NASA Langley 12-Foot Tunnel, Test 141, July 5-25, 2004.

[15] "UAV *Thunderstruck:* Spring Report", NC State University Senior Aircraft Design Class: Spring Report, May 2002.

APPENDICES

Appendix A

MESA Shape Authorities and Predictions for C_L, C_m, and C_l

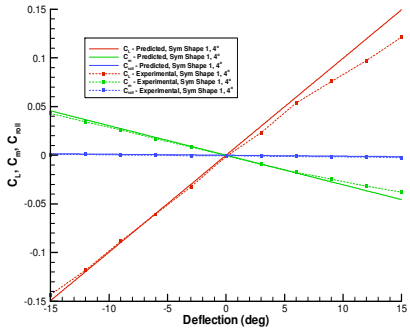

Figure A.1: Predictions of lift, pitch, and roll for symmetric shape 1 deflections at $\alpha = +4\,^\circ$.

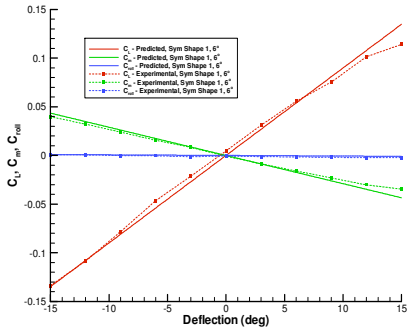

Figure A.2: Predictions of lift, pitch, and roll for symmetric shape 1 deflections at $\alpha = +6\,^\circ$.

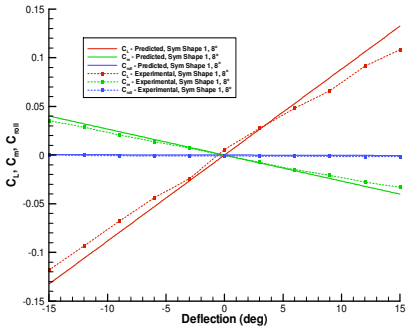

Figure A.3: Predictions of lift, pitch, and roll for symmetric shape 1 deflections at $\alpha = +8\,^{\circ}$.

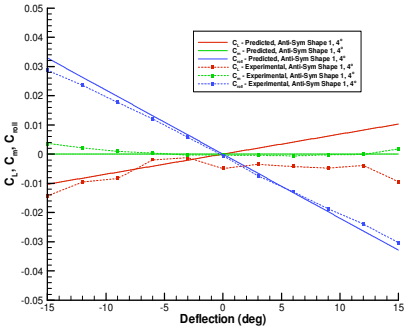

Figure A.4: Predictions of lift, pitch, and roll for anti-symmetric shape 1 deflections at $\alpha = +4\,^{\circ}$.

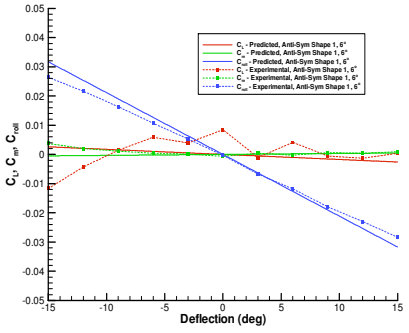

Figure A.5: Predictions of lift, pitch, and roll for anti-symmetric shape 1 deflections at $\alpha = +6\,^{\circ}$.

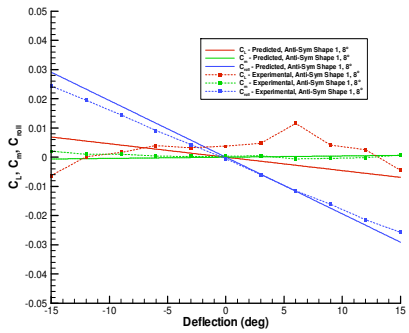

Figure A.6: Predictions of lift, pitch, and roll for anti-symmetric shape 1 deflections at $\alpha = +8\,^{\circ}$.

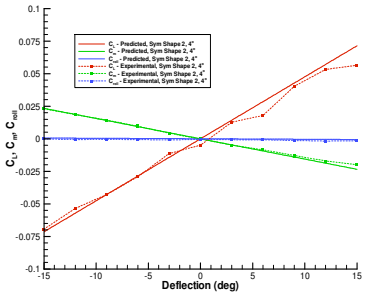

Figure A.7: Predictions for symmetric shape 2 deflections at $\alpha = +4\,^{\circ}$.

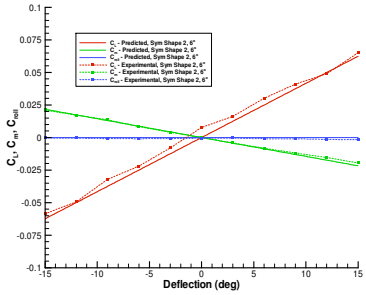

Figure A.8: Predictions for symmetric shape 2 deflections at $\alpha = +6\,^{\circ}$.

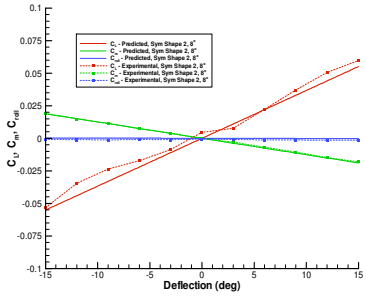

Figure A.9: Predictions for symmetric shape 2 deflections at $\alpha = +8\,^{\circ}$.

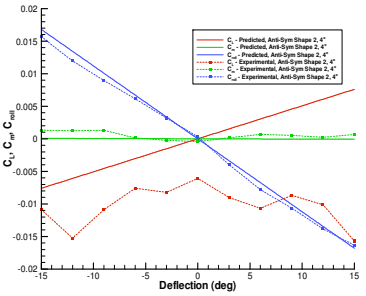

Figure A.10: Predictions for anti-symmetric shape 2 deflections at $\alpha = +4\,^{\circ}$.

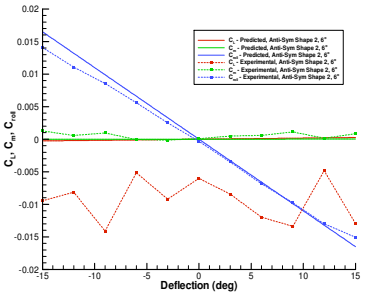

Figure A.11: Predictions for anti-symmetric shape 2 deflections at $\alpha = +6\,^{\circ}$.

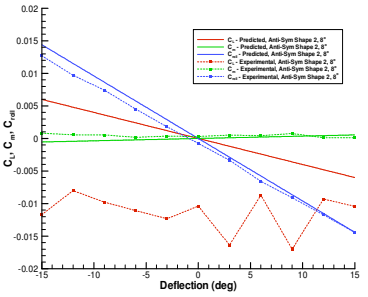

Figure A.12: Predictions for anti-symmetric shape 2 deflections at $\alpha = +8\,^{\circ}$.

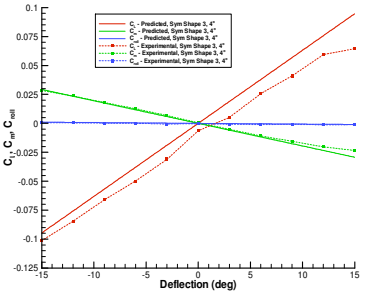

Figure A.13: Predictions for symmetric shape 3 deflections at $\alpha = +4\,^\circ$.

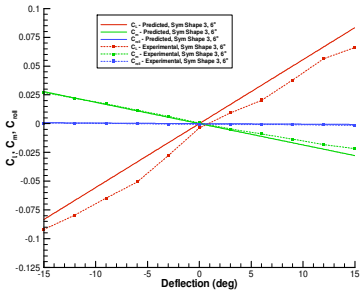

Figure A.14: Predictions for symmetric shape 3 deflections at $\alpha = +6\,^\circ$.

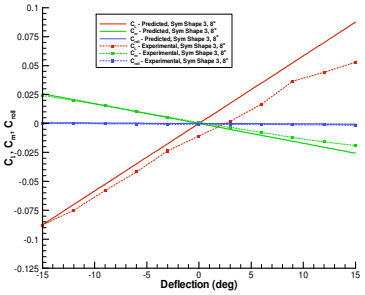

Figure A.15: Predictions for symmetric shape 3 deflections at $\alpha = +8\,^\circ$.

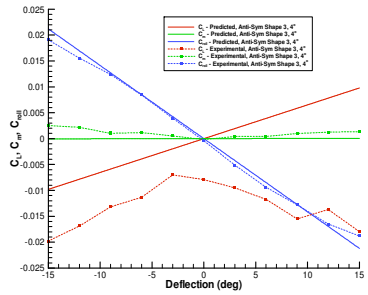

Figure A.16: Predictions for anti-symmetric shape 3 deflections at $\alpha = +4\,^\circ$.

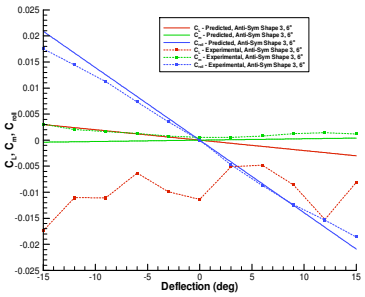

Figure A.17: Predictions for anti-symmetric shape 3 deflections at $\alpha = +6\,^\circ$.

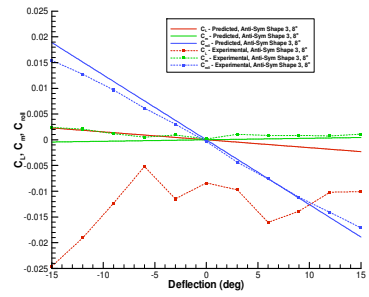

Figure A.18: Predictions for anti-symmetric shape 3 deflections at $\alpha = +8\,^\circ$.

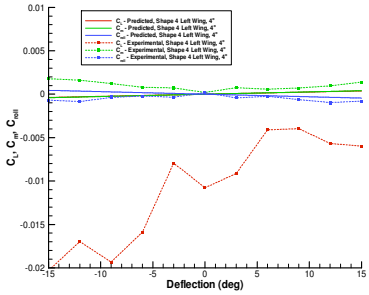

Figure A.19: Predictions for left wing shape 4 deflections at $\alpha = +4\,^{\circ}$.

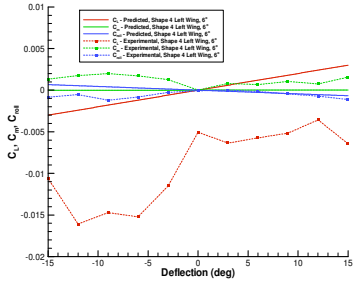

Figure A.20: Predictions for left wing shape 4 deflections at $\alpha = +6\,^{\circ}$.

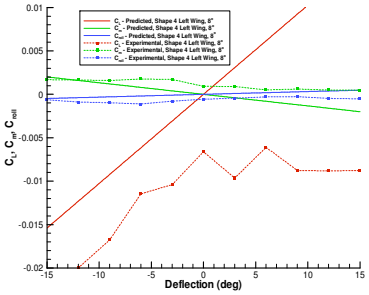

Figure A.21: Predictions for left wing shape 4 deflections at $\alpha = +8\,^{\circ}$.

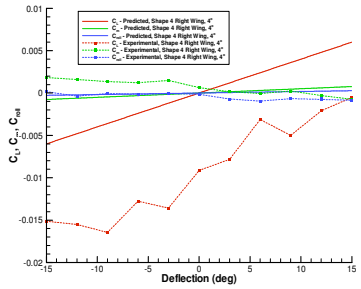

Figure A.22: Predictions for right wing shape 4 deflections at $\alpha = +4\,^{\circ}$.

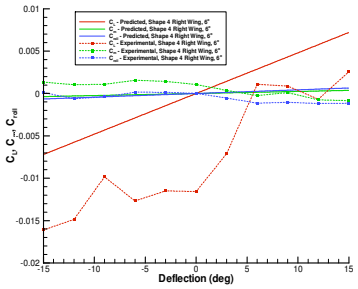

Figure A.23: Predictions for right wing shape 4 deflections at $\alpha = +6\,^{\circ}$.

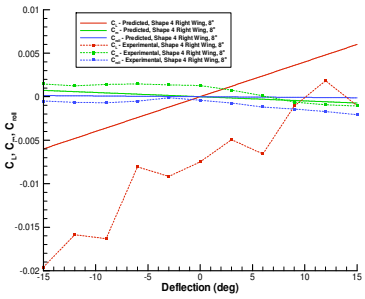

Figure A.24: Predictions for right wing shape 4 deflections at $\alpha = +8\,^{\circ}$.

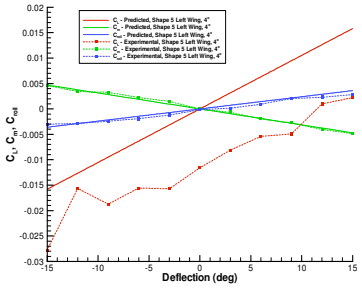

Figure A.25: Predictions for left wing shape 5 deflections at $\alpha = +4\,^{\circ}$.

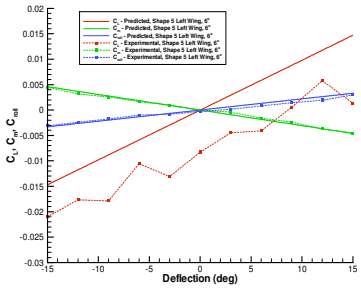

Figure A.26: Predictions for left wing shape 5 deflections at $\alpha = +6\,^{\circ}$.

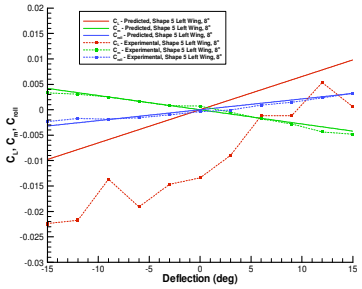

Figure A.27: Predictions for left wing shape 5 deflections at $\alpha = +8\,^{\circ}$.

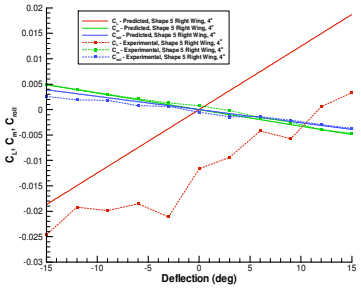

Figure A.28: Predictions for right wing shape 5 deflections at $\alpha = +4\,^{\circ}$.

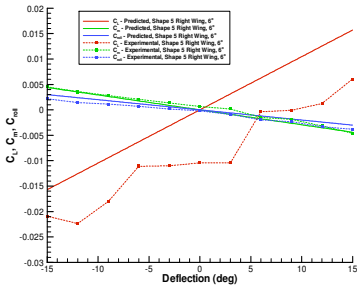

Figure A.29: Predictions for right wing shape 5 deflections at $\alpha = +6\,^{\circ}$.

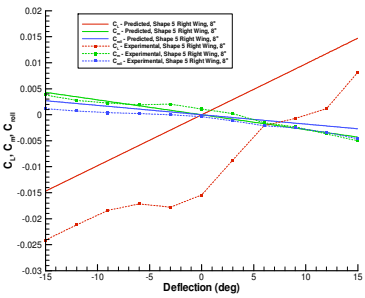

Figure A.30: Predictions for right wing shape 5 deflections at $\alpha = +8\,^{\circ}$.

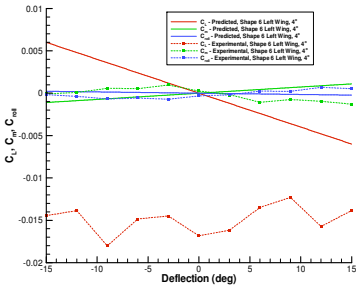

Figure A.31: Predictions for left wing shape 6 deflections at $\alpha = +4\,^{\circ}$.

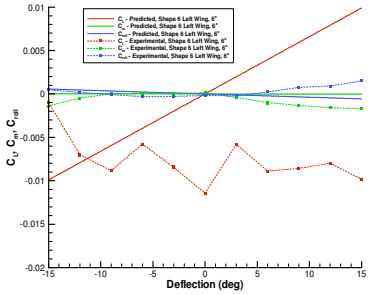

Figure A.32: Predictions for left wing shape 6 deflections at $\alpha = +6\,^{\circ}$.

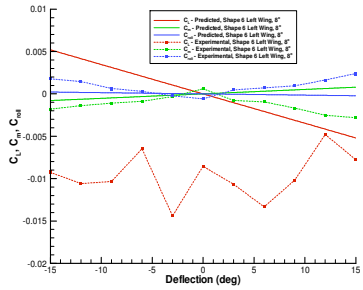

Figure A.33: Predictions for left wing shape 6 deflections at $\alpha = +8\,^{\circ}$.

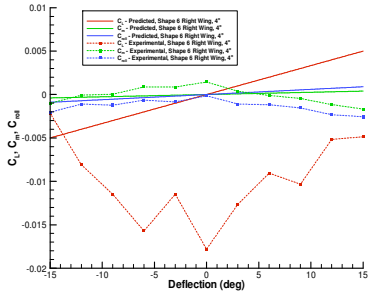

Figure A.34: Predictions for right wing shape 6 deflections at $\alpha = +4\,^{\circ}$.

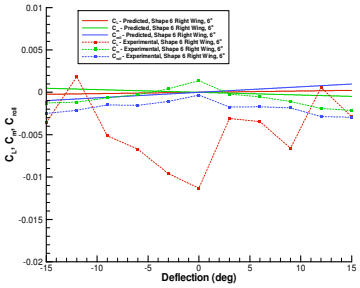

Figure A.35: Predictions for right wing shape 6 deflections at $\alpha = +6\,^{\circ}$.

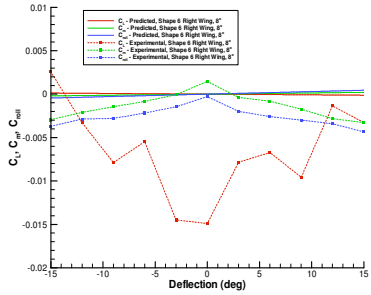

Figure A.36: Predictions for right wing shape 6 deflections at $\alpha = +8\,^{\circ}$.

Appendix B

MESA Shape Authorities and Predictions for C_D and C_n

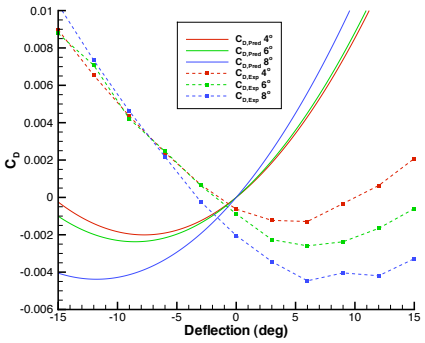

Figure B.1: Predictions of drag for symmetric shape 1.

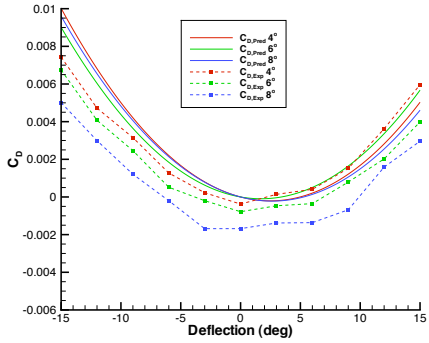

Figure B.2: Predictions of drag for anti-symmetric shape 1.

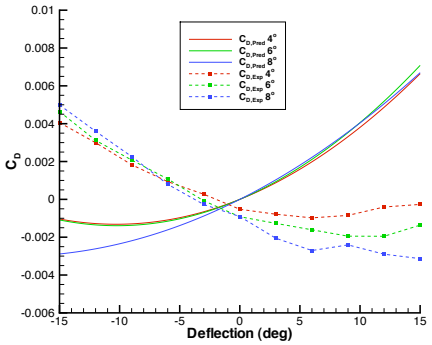

Figure B.3: Predictions of drag for symmetric shape 2.

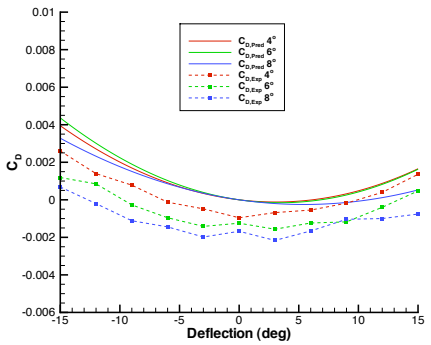

Figure B.4: Predictions of drag for anti-symmetric shape 2.

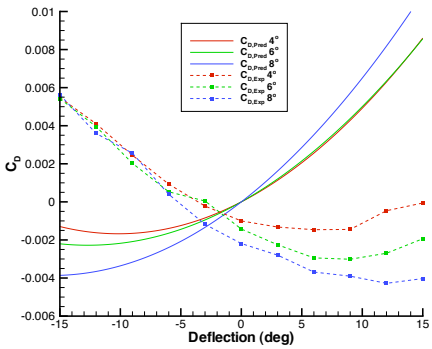

Figure B.5: Predictions of drag for symmetric shape 3.

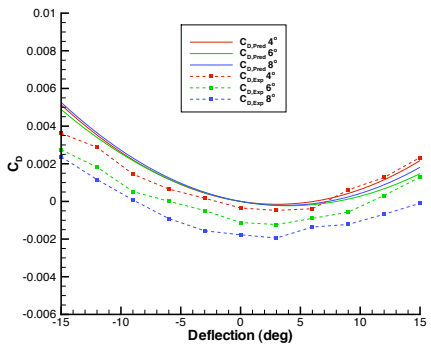

Figure B.6: Predictions of drag for anti-symmetric shape 3.

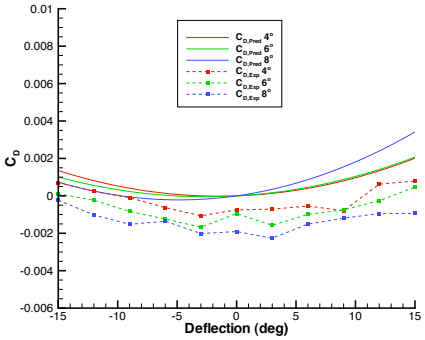

Figure B.7: Predictions of drag for left wing shape 4.

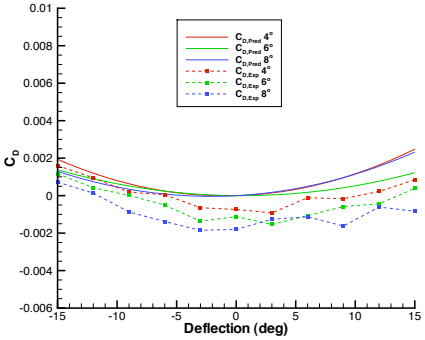

Figure B.8: Predictions of drag for right wing shape 4.

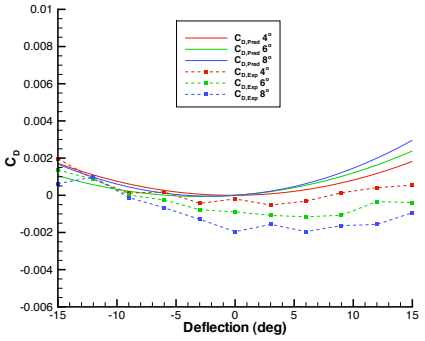

Figure B.9: Predictions of drag for left wing shape 5.

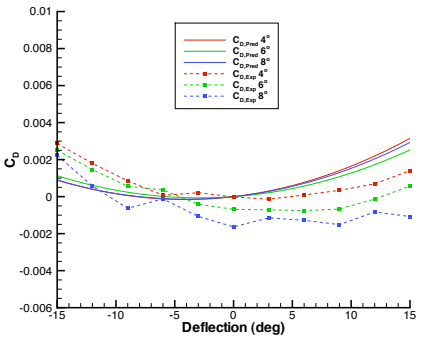

Figure B.10: Predictions of drag for right wing shape 5.

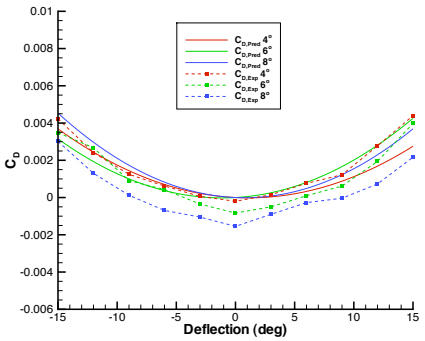

Figure B.11: Predictions of drag for left wing shape 6.

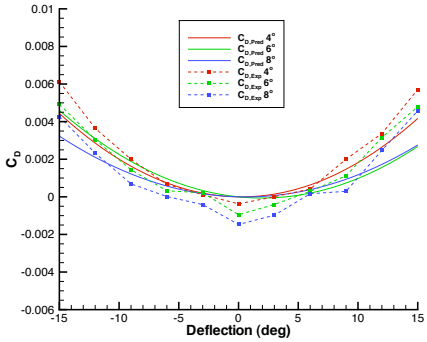

Figure B.12: Predictions of drag for right wing shape 6.

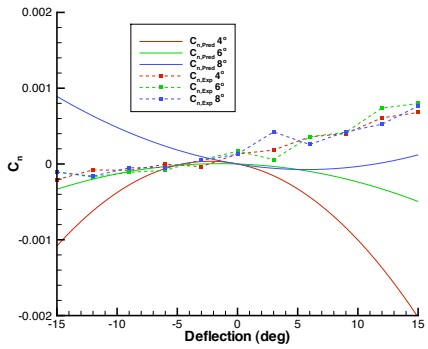

Figure B.13: Predictions of yaw for symmetric shape 1.

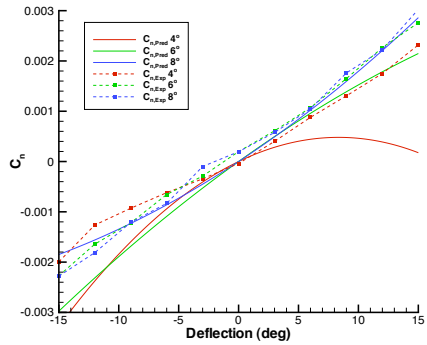

Figure B.14: Predictions of yaw for anti-symmetric shape 1.

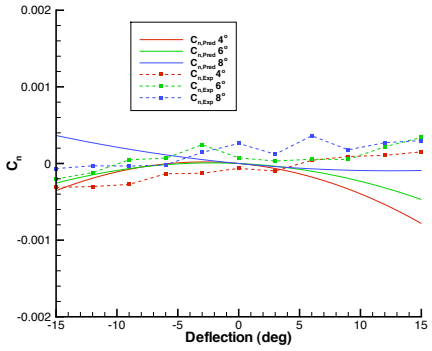

Figure B.15: Predictions of yaw for symmetric shape 2.

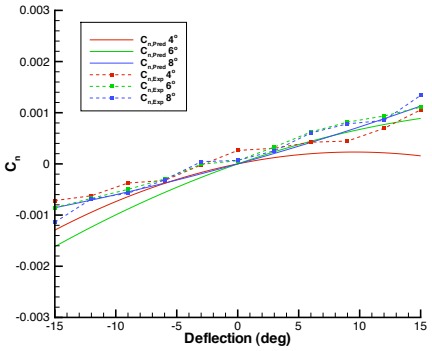

Figure B.16: Predictions of yaw for anti-symmetric shape 2.

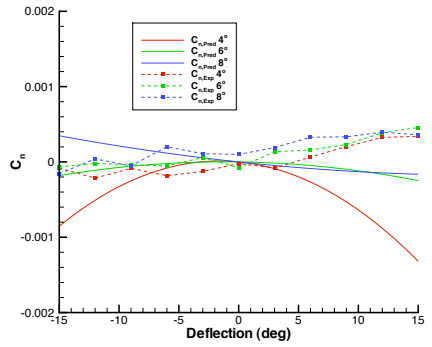

Figure B.17: Predictions of yaw for symmetric shape 3.

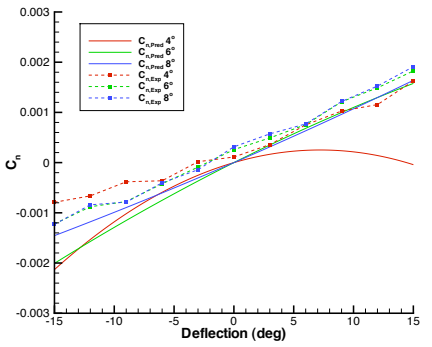

Figure B.18: Predictions of yaw for anti-symmetric shape 3.

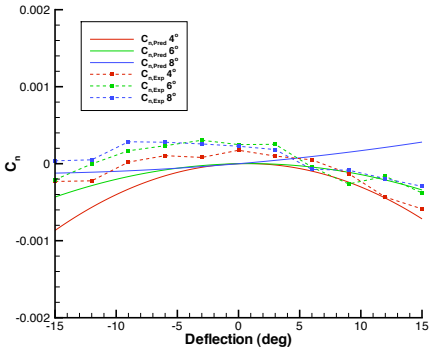

Figure B.19: Predictions of yaw for left wing shape 4.

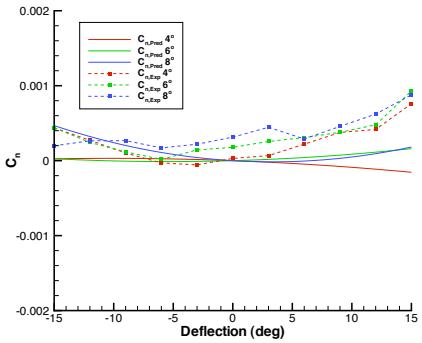

Figure B.20: Predictions of yaw for right wing shape 4.

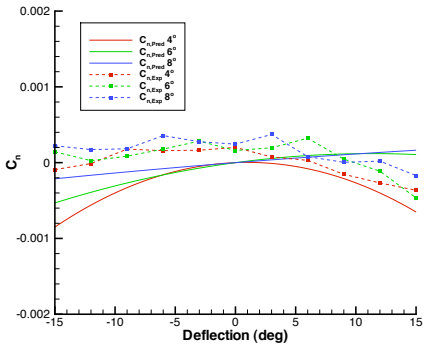

Figure B.21: Predictions of yaw for left wing shape 5.

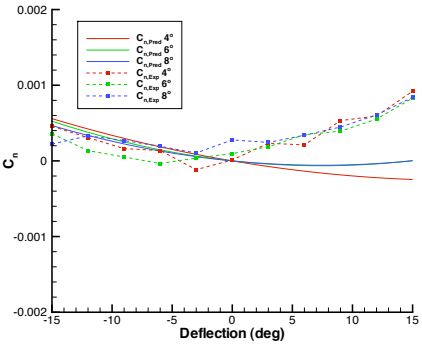

Figure B.22: Predictions of yaw for right wing shape 5.

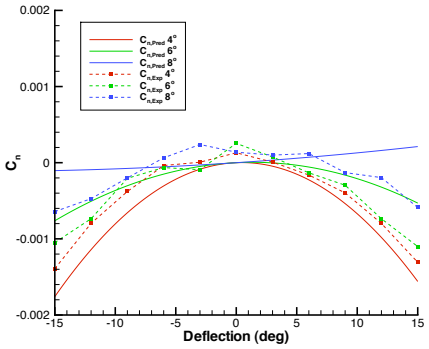

Figure B.23: Predictions of yaw for left wing shape 6.

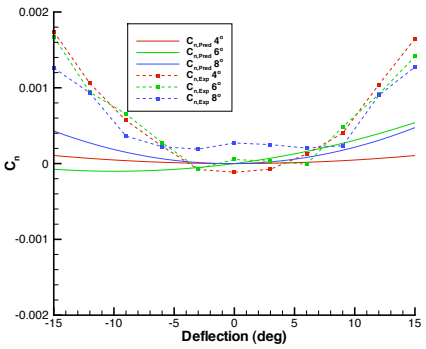

Figure B.24: Predictions of yaw for right wing shape 6.

Appendix C

MESA Shape Predictions for C_D Using Yaw Method

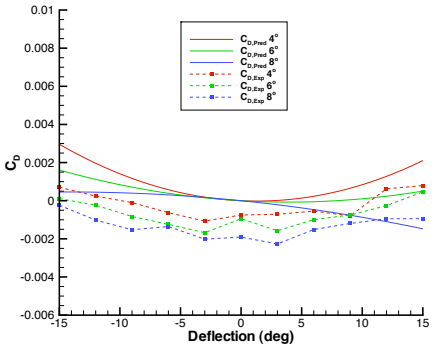

Figure C.1: Predictions of drag for left wing shape 4 using yaw method.

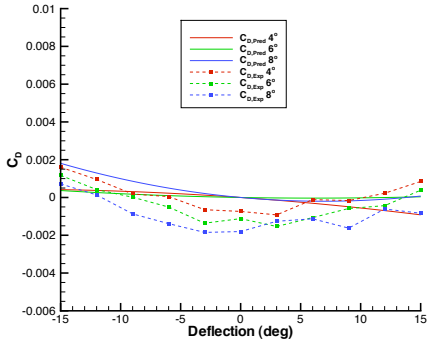

Figure C.2: Predictions of drag for right wing shape 4 using yaw method.

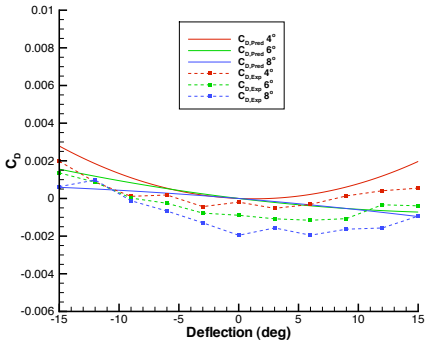

Figure C.3: Predictions of drag for left wing shape 5 using yaw method.

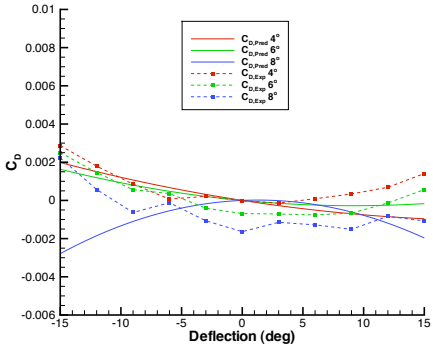

Figure C.4: Predictions of drag for right wing shape 5 using yaw method.

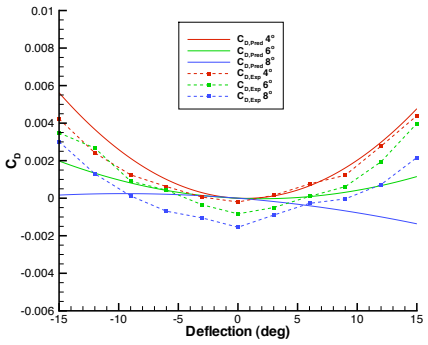

Figure C.5: Predictions of drag for left wing shape 6 using yaw method.

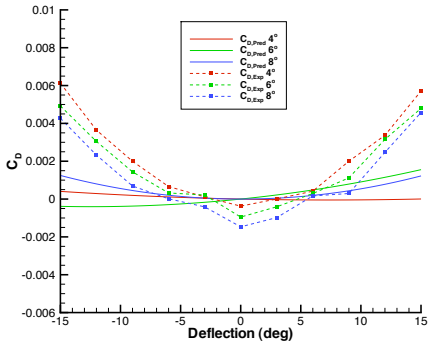

Figure C.6: Predictions of drag for right wing shape 6 using yaw method.